

Entropic phase separation in polymer–vitriimer melts

Alexandros A. Rispo Constantinou ^{*1,2}, Bálint Magyari ^{1,3}, Giovanni Ianniruberto ¹,
Evelyne van Ruymbeke ², and Daniel J. Read ⁴

¹DICMaPI, Università degli Studi di Napoli Federico II, 80125 Naples, Italy

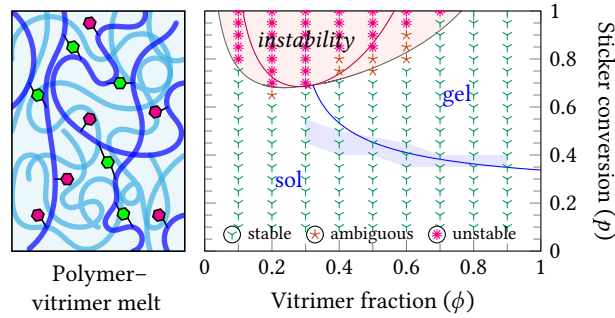
²BSMA, IMCN, Université catholique de Louvain, 1348 Louvain-la-Neuve, Belgium

³MSE, University of Crete, 70013 Heraklion, Greece

⁴School of Mathematics, University of Leeds, Leeds LS2 9JT, United Kingdom

*E-mail: alexandrosandreas.constantinou@unina.it

25th March 2026



Abstract

Traditional plastics demand a choice between durability (thermosets) and reprocessability (thermoplastics). Vitrimers are a recent class of polymer network combining both these qualities. Their increased cost of production can be offset by mixing them with a traditional thermoplastic; however, phase separation in such blends can lead to inhomogeneous materials. In this paper, we adapt an existing model for the free energy of dissociative polymer networks to their associative, vitriimer counterpart. We test the accuracy of the model’s predictions by comparing them with the results of novel molecular-dynamics simulations. We demonstrate that such melts can undergo phase separation even in the absence of energetic interactions between the components. We find furthermore that the phase diagram of the melts is qualitatively similar to that of dissociative systems, and that the critical degree of conversion for the onset of phase separation depends reciprocally on the number of function sites per vitriimer chain.

Keywords vitrimers, vitriimer blends, entropy-driven phase separation, associative covalent adaptive networks (asso-CANs), dynamic polymer networks (DPNs)

Résumé

Traditionnellement, le plastique était soit durable, soit recyclable : soit thermodurci, soit thermoplastique. Les vitrimères sont une récente catégorie de matériau unissant ces deux qualités. Leur coût de production plus élevé peut être compensé en les mêlant à un polymère thermoplastique ; cependant, les mélanges vitrimère/polymère sont susceptibles à la démixtion, ainsi présentant un obstacle à l'obtention de mélanges homogènes. Cet article prend un modèle pré-existant pour l'énergie libre de réseaux polymériques dissociatifs et l'adapte au cas vitrimérique, à réticulation associative. Afin d'en évaluer la fiabilité, les prédictions du modèle sont ensuite comparées aux résultats de nouvelles simulations de dynamique moléculaire. Nous constatons que les mélanges vitrimère/polymère peuvent subir une séparation de phase même sans interactions énergétiques entre leurs composantes. De plus, le diagramme de phases obtenu théoriquement est semblable à celui de systèmes dissociatifs, avec la particularité que le taux de conversion critique pour la présence de démixtion dépend inversement du nombre de sites fonctionnels par chaîne vitrimérique.

Mots clef vitrimères, mélanges vitrimériques, séparation de phase, démixtion entropique, réseaux covalents adaptables associatifs, réticulation polymérique dynamique

Sommario

Le plastiche tradizionali esigono una scelta tra durabilità (polimeri termoindurenti) e riciclabilità (termoplastici). I vitrimeri, invece, sono una recente classe di materiali che conciliano entrambe le qualità. Il loro maggiore costo di produzione può essere compensato immettendoli in una matrice termoplastica tradizionale; tuttavia, lo smiscelamento spontaneo per via di separazione di fase è un ostacolo importante alla preparazione di miscele omogenee vitrimero-polimeriche. In questo articolo, si adatta un modello preesistente per l'energia libera di un reticolo polimerico associativo al caso vitrimero, esso dissociativo. Si sonda poi la validità del modello confrontandone le previsioni con i risultati di simulazioni di dinamica molecolare originali. Si dimostra che tali fusi vitrimero-polimerici possono subire separazione di fase anche in assenza di interazioni energetiche tra le loro componenti, e che il diagramma di fase del fuso è qualitativamente simile al suo analogo dissociativo. Infine, si scopre che il grado di conversione critico per lo sviluppo di separazione di fase dipende inversamente dal numero di siti funzionali sulle catene vitrimeriche.

Parole chiave vitrimeri, fusi vitrimERICI, separazione di fase, smiscelamento entropico, reticoli covalenti adattabili associativi, reticoli polimerici dinamici

1 Introduction

Fifteen years ago, Leibler and co-workers (Montarnal et al., 2011) first stably synthesised a new class of materials they dubbed ‘vitrimers’. These materials have a wide variety of applications (Denissen et al., 2016; Zheng et al., 2021), which include their use as a recyclable, self-healing alternative to thermosets; as a compatibiliser providing reversible adhesion between immiscible materials; or, mixed with a classical homopolymer, as an additive to improve thermomechanical properties without loss of reprocessability (Torres et al., 2026; Wang et al., 2021). They achieve this remarkable versatility by forming polymer networks much like a thermoset, with a fixed number of cross-links, but capable of reversibly reshuffling cross-link sites to rearrange the network topology. Vitrimers are built from functional copolymers, typically obtained from commercially available monomers with the periodic addition of pendant functional groups (*i. e.*, cross-link-capable sites). A small cross-linking molecule is then added, forming covalent bonds with the functional sites; being highly energetic, these bonds are rarely broken at normal temperatures. However, they can exchange attachment points with other cross-linkers, and do so often, as this reaction has fairly low energy of activation (Winne et al., 2019). Sites not occupied by cross-linkers are stoppered by some ‘stopper’ moiety, which acts as a place-holder to prevent empty sites from reacting haphazardly. The only reaction present in the final material is thus the exchange of attachment points between moieties (cross-linker–cross-linker and cross-linker–stopper). In this way, a dynamic network is formed which rearranges itself topologically yet always maintains a constant overall number of cross-links.

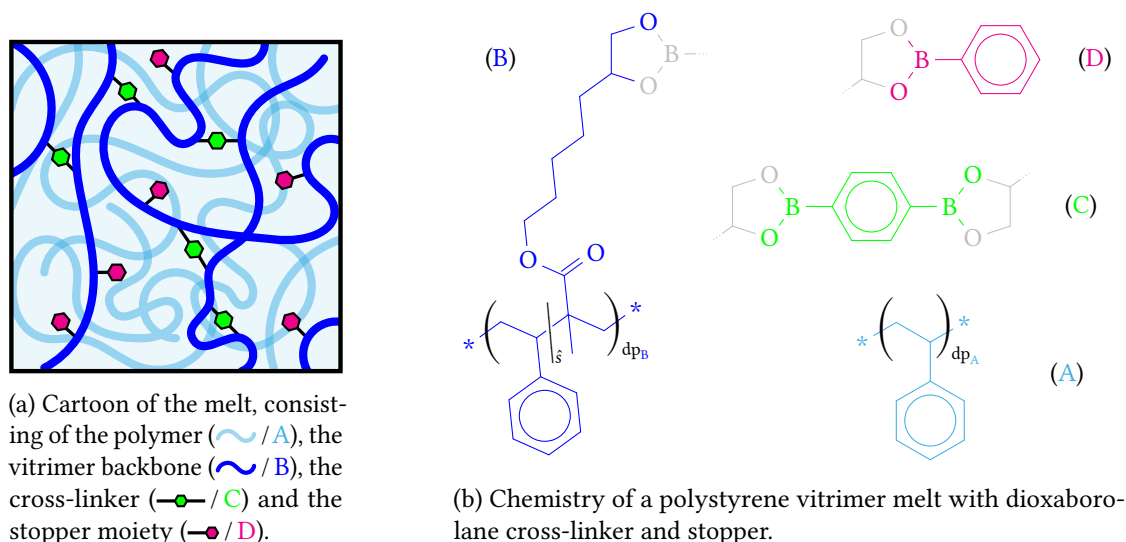


Figure 1: Anatomy of a vitrimer–homopolymer melt.

One application of particular interest involves dispersing vitrimers into a classical homopolymer matrix. By carefully selecting the materials involved, the resulting mixture can be made more thermomechanically resistant than a traditional thermoplastic, at a fraction of the cost of a pure vitrimer. Unlike a thermoset with permanent cross-links, this hybrid material

is reprocessable and self-healing, thanks to the cross-links' dynamic nature. The anatomy of such a mixture — in the specific case of a polystyrene vitrimer with dioxaborolane moieties — is illustrated in fig. 1. Therein, the cross-linker moiety (C) attaches to functional sites on the vitrimer backbone (B), and the stopper moiety (D) is simply a monofunctional version of the cross-linker, filling up all remaining sites. The fourth component is the matrix (A), which we refer to interchangeably as polymer or homopolymer.

Studies of such melts are still scarce. However, preliminary evidence suggests that such melts do not mix homogeneously. A study of poly(methyl methacrylate) in an epoxy vitrimer matrix (Han and Xu, 2018) finds clear micron-scale phase separation when the mix is equal parts by weight. Analyses of pure vitrimers (Hayashi, 2025; Ricarte et al., 2019) also detect traces of phase separation at several scales; see de Heer Kloots et al. (2023) for a detailed qualitative discussion. Controlling micro-structure is important for the practical use of vitrimers: some applications call for well-mixed melts; others rely on specific modes of phase separation (Joosten et al., 2024). Currently, achieving the correct micro-structure relies on repeatedly iterating experiments and prototypes, a procedure both costly and time-consuming. There is thus a need for a predictive approach to phase separation, which can be achieved through an appropriate theoretical model.

Classical theories of adaptive polymer networks apply to 'dissociative' systems, where the functional sites detach and reattach without the intermediary of cross-linker or stopper moieties. This phenomenon is governed by the energy of association, which is the energy respectively lost or gained by forming or breaking a bond. As such, dissociative networks create or destroy cross-links at will, thereby freely altering their connectivity properties. Since bonds can associate and dissociate, the actual number of bonds (i) will fluctuate around the mean fraction for a material at equilibrium, (ii) may evolve with time when out of equilibrium, and (iii) may not be conserved during processes such as phase separation — in other words, the total number of bonds may change. The mean fraction of bonds associated at any given time is called the 'degree of conversion' (p), and can be predicted at equilibrium by minimising the free energy of the dissociative system. The result depends on the energy of association as well as on the composition of the mixture; it also varies with temperature, with hotter samples exhibiting fewer bonds (lower p) on average.

In contrast, vitrimers — or 'associative' systems — exist in the limit of high energy of association, when it is almost never favourable to break a bond. This justifies the assumption that, in vitrimers, the total degree of conversion is a conserved quantity: in this approximation, cross-links can change attachment sites, but can never detach spontaneously. A consequence is that vitrimer systems can be treated purely entropically: since the number of bonds remain fixed, the total bonding energy remains constant; hence, it is possible to conceive of an idealised, entropic vitrimer system whose state depends only on the number of microstates generated by the presence of bonds and different chain configurations. Although real vitrimer blends almost certainly also involve energetic effects (*e. g.* from interaction parameters), it is instructive to investigate first the ideal, entropic case. Therefore, we will restrict the scope of this paper to systems governed entirely by entropic effects, without energetic interactions between any of the four component moieties A–D (*c. f.* fig. 1).

Existing theories mostly describe dissociative networks; nonetheless, similar systems have been extensively studied in the theoretical literature. Approaches include mean-field theory (Dobrynin, 2004; Semenov and Rubinstein, 1998), a patchy-particle model (Smallenburg et al., 2013), coherent-state field theory (Vigil et al., 2025), cluster expansions (Fantoni and Müller-Nedebock, 2011) and more; see Tanaka (2022) for a review of the literature. The mean-field theory due to Semenov and Rubinstein (1998) and expanded by Dobrynin (2004) is a popular framework. It has been used to study solutions of polyelectrolytes (Chen et al., 2025), blends of heteroassociative polymers (Danielsen et al., 2023), mixtures of polymers with compatible functional sites (Prusty et al., 2018), and has been to an extent compared with experiments (Skorik et al., 2016). This approach has the advantage of producing a free-energy function from counting arguments alone, without invoking heavy mathematical artillery. In this paper, we use this framework to arrive at a phase diagram of vitrimer–polymer melts in the absence of enthalpic effects. We will find similar qualitative predictions to those of dissociative systems (Dobrynin, 2004; Semenov and Rubinstein, 1998), namely that macro-phase separation occurs whenever the degree of conversion (resp. energy of association) is sufficiently large. In contrast with the dissociative case, however, there are compositions of melt which never undergo separation (generally if the proportion of vitrimer is sufficiently large or small). Furthermore, the separation we predict is fully driven by the entropy of the resulting phases, meaning that it is a purely statistical phenomenon.

Our work addresses the need for a predictive model of phase separation in vitrimer–polymer melts by providing an initial, simplistic description using the mean-field theory. Thus far, no systematic experimental campaign has been conducted to capture regimes of stability in these melts. To validate our description, we therefore turn to numerical methods. Molecular dynamics simulations have been used extensively to model polymer systems (Behbahani and Schmid, 2025; Everaers et al., 2020; Kremer and Grest, 1990); by adding Monte-Carlo-based interactions between selected beads, they have successfully been extended to model dynamic polymer networks (Cui et al., 2023; Perego, Lazarenko et al., 2022; Xia et al., 2023). While Monte-Carlo simulations have been used extensively to study the *viscoelastic* behaviour of vitrimer melts, phase separation remains largely unexplored territory. To our knowledge, this study constitutes the first systematic comparison with simulations of the mean-field-type theory introduced by Semenov and Rubinstein (1998).

The goal of this paper is, therefore, to provide a combined theoretico-simulative approach to predicting macroscopic phase separation in vitrimer–polymer melts, meant to guide experimental exploration of these materials’ design space. The paper is structured as follows. In section 2, we derive a mathematical model for the free energy of a vitrimer–polymer melt devoid of energetic interactions. Section 3 then presents the hybrid Monte-Carlo / molecular-dynamics simulative approach adopted to validate the theory. In section 4, we compare simulation results with the theoretically predicted incidence of macroscopic phase separation, and discuss possible extensions of the theory. Conclusions are drawn in section 5.

2 Free energy model

In this section, we derive the Helmholtz free energy for a vitrimer–polymer melt. For the sake of exposition, we will only present a simplified derivation where the small moieties – cross-linker and stopper – are ‘phantom objects’ which do not occupy any volume. (A complete derivation with this assumption lifted is given in the supplementary information, appendix A.) The resulting model assumes that the functionalised monomers on every vitrimer chain can directly bond to other functionalised monomers, without the intermediary of a physical cross-linker. We will use the language of previous works on dissociative polymer networks and call these special monomers ‘stickers’, and define a sticker as ‘bonded’ if the equivalent functional site is attached to a cross-linker, and ‘free’ otherwise (table 1). Though confusing at first, this change in language allows better alignment with existing literature, and makes the link to simulations more straightforward.

Chemical nomenclature	Phantom model
Functional site	Sticker
Site with cross-link	Bonded sticker
Site with stopper	Free sticker

Table 1: Conversion between terminologies.

Therefore, the melt consists of two species: a homopolymer matrix, chemically inert, and a vitrimeric network of the same chemical nature, every chain of which has s designated stickers. We assume that stickers are uniformly distributed along the chain (*i. e.*, located at equal monomeric intervals), with half an interval at the extremities. To emulate the effect of covalent bonds, we fix the total number of sticker–sticker cross-links (‘bonds’) to some global value. Since the number of bonds is fixed, and the vitrimer and homopolymer are assumed not to interact energetically, all microstates have the same enthalpy, and the internal energy may be excluded from the computation of the partition function. The calculation thus involves only a conformational or entropic term, counting the number of ways to arrange vitrimer and polymer chains in the melt. The predictions of this simplified model will be shown at the end of section 2.4, and later compared to the results of simulations in section 4.1.

2.1 Derivation

We follow in large part the derivation of Semenov and Rubinstein (1998), rewritten in terms of a lattice model. The major difference is that we do not approximate the solvent’s effect through its virial coefficients, given that our ‘solvent’ is actually a polymer matrix. Our basic theory, before the addition of cross-links, is the classical Flory–Huggins theory of polymer melts.

To obtain the partition function, we count the number of ways of arranging the vitrimer and polymer chains on a lattice, subject to the constraint of forming the correct number of sticker–sticker bonds. We start by giving the number of ways of arranging the chains in the absence of such constraints, Ω_{FH} , and later correct it by a combinatorial factor.

Given a lattice of n_0 sites filled with n vitrimer chains, each occupying N sites, and m polymer chains, each occupying M sites, the number of ways of placing these chains on the lattice is given in the mean-field approximation by

$$\Omega_{\text{FH}} := \frac{n_0!}{n_0^{n_0}} \frac{(n_0 \zeta_N)^n}{n!} \frac{(n_0 \zeta_M)^m}{m!}, \quad (1)$$

where the ζ_i represent the number of internal configurations available to the chains on the lattice, uncorrected for excluded volume; hence the explicit dependence on N and M in ζ_N and ζ_M . Equation (1) is a standard result of the Flory–Huggins theory; its derivation can be found in Flory (1953) or, for convenience, in the supplementary information (appendix A).

If there are c cross-links between stickers (one cross-link for two stickers), the partition function Ω_{FH} needs to be multiplied by the number of ways of forming c distinct sticker pairs, as well as by the probability that the chains are in a configuration allowing that many bonds. Forming c pairs out of $s \times n$ stickers is equivalent to ordering the stickers in a list defined such that the first sticker is paired with the second, the third with the fourth, and so on. The remaining $sn - 2c$ stickers are unpaired. The following diagram illustrates the situation, with each sticker represented by an asterisk (*).

$$\underbrace{(*, *) (*, *) \dots (*, *)}_{\substack{2c \text{ stickers} \\ \text{form } c \text{ pairs}}} \quad \Bigg| \quad \underbrace{*** ** \dots *}_{\substack{sn-2c \text{ stickers} \\ \text{remain unpaired}}}$$

There are $(sn)!$ ways of arranging the stickers in this list, to be corrected by dividing by $c!$ (since the ordering of the pairs doesn't matter), by $(sn - 2c)!$ (since the ordering of the unpaired stickers doesn't matter), and by 2^c (since the ordering of the stickers within a pair doesn't matter).

Next we compute the probability that the chains be in a configuration allowing c bonds. A given bond is allowed if and only if that bond's second sticker occupies one of the x sites on the immediate coordination shell of the first sticker. This happens with probability x/n_0 . The event then needs to recur c times, so the probability becomes $(x/n_0)^c$. (The number of cross-link-compatible second sites x depends on the specific geometry of the chains, but is usually taken to be two less than the lattice coordination number, accounting for monomers adjacent to the sticker.)

The full partition function Ω is thus the product of these two factors with Ω_{FH} , namely

$$\Omega = \Omega_{\text{FH}} \times \frac{(sn)!}{2^c c! (sn - 2c)!} \times \left(\frac{x}{n_0} \right)^c. \quad (2)$$

To obtain an expression for the entropy, we apply Stirling's formula $z! \sim (z/e)^z$ and take the natural logarithm of Ω . We also wish to rewrite the expression in terms of (independent) intensive variables: one is the volume fraction occupied by vitrimer chains, $\phi := Nn/n_0$; the other is a rescaled version of the volume fraction occupied by bonded stickers: $\psi := 2c/n_0 \times N/s$. We choose the scaling factor N/s on this second quantity so that ψ ranges between zero and ϕ , and the degree of conversion of stickers is $p := 2c/sn = \psi/\phi$. The volume fraction occupied by the polymer is — by conservation of volume — not an independent variable, and indeed

is equal to $1 - \phi = Mm/n_0$. Performing these substitutions, and defining $\mathfrak{H}(z) := z \log(z)$ for compactness, the non-dimensional free energy per lattice site $f := -\log(\Omega)/n_0$ is given by

$$\frac{N}{s} f \approx \frac{1}{s} \left[\mathfrak{H}(\phi) + \frac{N}{M} \mathfrak{H}(1 - \phi) \right] + \mathfrak{H}(\phi - \psi) + \frac{1}{2} \mathfrak{H}(\psi) - \mathfrak{H}(\phi). \quad (3)$$

Here and elsewhere in the text we have freely removed from the free energy both constants and terms linear in the concentration variables (ϕ, ψ) , as they have no effect on the resulting predictions (*c.f.* section 2.4). It is worth emphasising that the expression Nf/s in eq. (3) is independent of any lattice parameters. Note also that the behaviour of the system does not directly depend on the lengths of the component chains, but only on their ratio M/N .

Heuristically, this expression for the free energy can be seen as the interplay between two competing influences: the first term in parentheses – scaling as $1/s$ – is convex, encouraging stable behaviour, whereas the rest of the expression pushes for instability. As s increases, the unstable influence becomes more prominent and the region of instability grows, leaving only a small island of stability near $(\phi, \psi) = (1, 0)$.

A variant derivation, due to Dobrynin (2004), suggests that the expression in eq. (3) takes into account the presence of cycles in the network; the details of this, along with the full derivation for volume-occupying cross-linker and stopper, are given in the supplementary information (appendix A).

2.2 Nearest-neighbour correction

The partition function provided in eq. (2) assumes that the second sticker within each pair has equal probability of lying anywhere in the system volume. Whilst good for stickers disconnected from each other (or only connected through a long enough path), this assumption is deficient when stickers are separated by short lengths of vitrimer backbone. In this case, the stiffness of the chains affects sticker distributions. The effect is particularly salient when the vitrimer is dilute in the matrix, and stickers mostly see stickers from the same chain in their immediate vicinity. Following both Dobrynin (2004) and Semenov and Rubinstein (1998), we model these local bonds through their leading-order behaviour, when stickers pair with their nearest neighbour along the chain (fig. 2). Longer-range bonds are polynomially suppressed by the entropic cost of forming a loop in the polymer, with scaling (loop length) $^{-3/2}$.

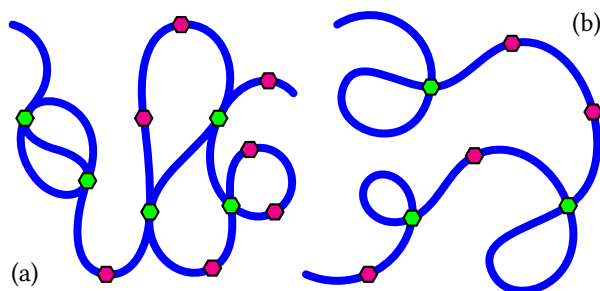


Figure 2: Generic same-chain linking (a) vs nearest-neighbour only (b).

First we calculate the contribution to the partition function due to nearest-neighbour bonds. Let a fraction q of the s stickers on a given vitrimer chain be involved in nearest-neighbour pairs. To calculate how many ways this can happen, imagine having a list of the $(s - qs)$ free stickers and $qs/2$ cross-linked sticker pairs on that chain, and asking the number of ways to rearrange these. By a ‘stars-and-bars’ argument (*e.g.* Levin, 2021), this is the same as taking $(s - qs) + qs/2$ objects, and selecting $qs/2$ to be pairs. The number of ways of doing this is simply the binomial coefficient $(s - qs/2)! / [(qs/2)! (s - qs)!]$. However, forming $qs/2$ nearest-neighbour pairs comes with an entropic cost, as the configurations that the two bonded stickers can have relative to each other are reduced. This cost can be accounted for by multiplying the partition function by the probability $\mathbb{P}[l_{N/s}]$ of forming a loop of length $l_{N/s}$, repeating as many times as there are loops ($qs/2$). The product of these two expressions is the amount by which each vitrimer chain modifies the partition function due to local bonds between nearest-neighbour stickers. For the full partition function, we multiply eq. (2) by n copies – one for each vitrimer chain – of this local-bond correction term. The result is

$$\Omega = \Omega_{\text{FH}} \times \left(\frac{(s - qs/2)!}{(qs/2)! (s - qs)!} \mathbb{P}[l_{N/s}]^{qs/2} \right)^n \times \left(\frac{x}{n_0} \right)^{\tilde{c}} \frac{(\tilde{s}n)!}{2^{\tilde{c}} \tilde{c}! (\tilde{s}n - 2\tilde{c})!}, \quad (4)$$

where $\tilde{s}n = sn - qsn$ and $\tilde{c} = c - qsn/2$ are the values reduced by the number of stickers (resp. cross-links) involved in local, nearest-neighbour pairs. As before, eq. (4) can be used to provide the free energy, yielding

$$\begin{aligned} \frac{N}{s} f = \frac{1}{s} & \left[\mathfrak{H}(\phi) + \frac{N}{M} \mathfrak{H}(1 - \phi) \right] + \mathfrak{H}(\phi - \psi) \\ & + \frac{1}{2} \mathfrak{H}(\psi - q\phi) - \mathfrak{H} \left(\left[1 - \frac{1}{2}q \right] \phi \right) \\ & + \frac{1}{2} \mathfrak{H}(q\phi) + \frac{1}{2} q\phi \log \left(\frac{2}{ke} \right). \end{aligned} \quad (5)$$

The first line is identical to its equivalent in eq. (3), the second line has an equivalent but now depends on q , and the third line is entirely new. We recover eq. (3) in the limit $q \rightarrow 0$, namely when all cross-links are to other vitrimer chains. (We have assumed so far that the cross-linker is two-sided: a similar expression to eq. (5) holds when the cross-linker is of arbitrary functionality; this derivation is given in the supplementary information, appendix C.)

In eq. (5), the fraction q of local cross-links is an unconstrained variable obeying only the inequality $q \leq p$. We therefore fix its value by extremising the free energy over q , namely by setting $\partial f / \partial q = 0$. The resulting optimality condition

$$\frac{(2 - q)q}{p - q} = \frac{k}{\phi} \quad (6)$$

is controlled by a parameter $k := \mathbb{P}[l_{N/s}] \times 4N / (sx)$ measuring the propensity for local bonding. Equation (6) can be solved to give

$$q = \frac{k + 2\phi}{2\phi} \left(1 - \sqrt{1 - \frac{4k\phi p}{(k + 2\phi)^2}} \right). \quad (7)$$

A good approximation is afforded by linearising q with respect to p , yielding $q \approx kp/(k+2\phi)$. This approximation is excellent so long as $4kp\phi/(k+2\phi)^2 \ll 1$; it is at its worst when $\phi = k/2$ and $p = 1$, with maximal error $3/2 - \sqrt{2}$, or about 9%. This error reduces quickly with decreasing p , being just over 5% by $p = 0.8$, and has little impact on the majority of the explored phase space; for typical values of p in practical applications, on the order of a few units per cent, the error is less than one in five thousand. This approximation greatly increased the speed in our numerical computation by facilitating evaluation of the free energy and its derivatives.

We see from the linearisation that the simpler expression in eq. (3) is most accurate when $k \rightarrow 0$, which occurs in the limit of greater inter-sticker spacing since $k \sim (N/s)^{-1/2}$ (see next section). Note also that as the solution becomes more dilute, we see q approach p : in other words, local bonds dominate the cross-linking behaviour, and percolation becomes increasingly difficult.

2.3 Local bonding propensity

The parameter k controlling the local bonding propensity remains a free parameter of this theory. Some intuition for it can be afforded by rephrasing it in terms of material properties of the vitrimer. In this section, we provide an interpretation through a simplified scaling argument then, for reference, perform the calculation exactly for ideal (Gaussian) vitrimer chains. The latter, exact result is not essential to the discussion.

Consider a segment of chain between two stickers, consisting of $l_{N/s}$ Kuhn segments, each of length b . To find $k := \mathbb{P}[l_{N/s}] \times 4N/(sx)$, we need the probability $\mathbb{P}[l_{N/s}]$ of the segment's two ends lying within a bond volume (v_b) of one another. This probability is proportional to the bond volume v_b when v_b is small, since the underlying segment-end distribution is approximately constant over small regions. The maximum value that the bond volume can take — at which the probability should be unity — scales as the cube of the chain segment's root-mean-square end-to-end radius $R_s \sim b\sqrt{l_{N/s}}$, which characterises the typical distance by which segment ends are likely to be separated. Thence the scaling $\mathbb{P}[l_{N/s}] \sim v_b/R_s^3$. Replacing the bond volume with its lattice-based equivalent $v_b = xv_0$, we obtain the scaling law $k \sim v_s/R_s^3$, where $v_s = v_0N/s$ is the volume taken up by the inter-sticker chain segment, or equivalently the volume of vitrimer chain per sticker. Interpreting R_s^3 as the volume spanned by the chain section between two stickers, we find that $1/k \sim R_s^3/v_s$ is (roughly) the typical number of stickers within a volume R_s^3 for a pure vitrimer system — *i. e.*, in the absence of a homopolymer matrix. Its square $1/k^2$ is also known as the ‘invariant degree of polymerisation’ (Qin, 2024) for that inter-sticker segment.

The packing length P of a polymer chain corresponds to the length scale on which a chain fully fills its pervaded volume, and is defined as the ratio of the chain's displaced volume to its root-mean-square end-to-end radius (Bobbili and Milner, 2021). Using the chain segment between adjacent stickers, we have $P \sim v_s/R_s^2$. The consequent scaling

$$k \sim P/R_s \tag{8}$$

gives a further intuitive interpretation of k as the reciprocal inter-sticker distance, measured in units of the packing length. This can be understood as encoding the fact that stickers within the same packing blob are easy to cross-link without losing much entropy; the more blobs they are separated by, however, the more costly (and therefore rare) cross-links become, and $k \rightarrow 0$.

For reference, we now compute k theoretically for an ideal chain (Doi and Edwards, 1988, § 2.3; Grosberg and Khokhlov, 1994, § 40.10). Recall that the Green's function $G_l(\vec{r})$ for an isolated phantom chain of l effective bonds of length b is given by the expression

$$G_l(\vec{r}) = \left(\frac{2\pi}{3}lb^2\right)^{-3/2} \exp\left(-\frac{3\|\vec{r}\|^2}{2lb^2}\right) \quad (9)$$

where \vec{r} is the end-to-end vector of the chain. Requiring that the chain ends lie within a volume v_b of one another is then equivalent to integrating over the locality operator $v_b \delta$, where δ is the Dirac delta. Thus

$$\mathbb{P}[l] = \int_{\mathbb{R}^3} d^3\vec{r} v_b \delta(\vec{r}) G_l(\vec{r}) = \frac{v_b}{b^3} \left(\frac{2\pi}{3}l\right)^{-3/2}. \quad (10)$$

The last step is then to express the inter-sticker distance in units of the effective bond length b . This is simply the number of Kuhn segments between successive stickers, obtained by dividing the volume $v_s = v_0 N/s$ of an inter-sticker chain segment by the volume v_K of a Kuhn segment, giving $l_{N/s} = N/s \times v_0/v_K$. Substituting all of these into $k := \mathbb{P}[l_{N/s}] \times 4N/(sx)$ and again replacing $v_b = xv_0$ gives

$$k = \frac{3\sqrt{6}}{\pi^{3/2}} \sqrt{\frac{s}{N}} \left(\frac{v_K}{\sqrt[3]{v_0} b^2}\right)^{3/2}, \quad (11)$$

with numerical prefactor about 1.34. In particular, note the scaling $k \sim \sqrt{s/N}$, implicit in eq. (8).

2.4 Phase diagram

From the free energy, we can obtain the phase diagram, displaying the system's behaviour for the entire phase space $(\phi, p) \in [0, 1]^2$, with $p = \psi/\phi$. We first describe how the various features of the diagram are computed, before presenting a typical phase diagram at the end of the section.

The spinodal curve is the transition from local stability to local instability, and occurs when the free energy goes from concave in both directions to convex in at least one; we find this curve by numerically searching for the zero contour of the Hessian determinant of the free energy $f = f(\phi, \psi)$. Namely, we solve

$$f_{,\phi\phi} f_{,\psi\psi} - (f_{,\phi\psi})^2 = 0, \quad (12)$$

where the subscript comma denotes differentiation with respect to subsequent variables. The binodal, marking the transition from true stability (global convexity) to a metastable state (locally convex but globally concave) is less straightforward, but is guaranteed to intersect the spinodal in at least one point; thence our methodology begins by obtaining this intersection, called the 'plait' or 'critical' point, by simultaneously solving the aforesaid spinodal condition eq. (12) along with an equation

$$f_{,\psi\psi\psi} f_{,\phi\psi} f_{,\phi\phi} - 3(f_{,\phi\psi})^2 f_{,\phi\psi\psi} + 3f_{,\phi\psi} f_{,\psi\psi\psi} f_{,\phi\phi\psi} - (f_{,\psi\psi\psi})^2 f_{,\phi\phi\phi} = 0 \quad (13)$$

specific to the plait point (Shcherbakova et al., 2023; Tompa, 1956, § 2.12; *qq. v*). Equation (13) corresponds to the statement that the plait point is an inflection point on the spinodal curve;

it can be derived from the condition $(\vec{t} \cdot \nabla)^3 f = 0$, where $\vec{t} \propto [-f_{,\phi\psi} \ f_{,\phi\phi}]^\top$ is any tangent to the spinodal and $\nabla := [\partial_\phi \ \partial_\psi]^\top$ is the differential operator on the phase space of conserved variables. Then, the binodal is found by imposing (and numerically solving for) equality of the chemical potentials $\mu_\phi := f_{,\phi}$, $\mu_\psi := f_{,\psi}$ and osmotic pressure $\Pi := \phi\mu_\phi + \psi\mu_\psi - f$ across both phases, according to the common-tangent construction. Straight-line segments joining such solutions are known as tie-lines, and conservation of the phase parameters (ϕ, ψ) implies that any unstable state lies on the tie-line into whose extremities it will separate. Therefore, we use a stepping algorithm to generate the tie-lines by guessing an unstable state and finding the tie-line passing through it, starting at the plait point and always moving perpendicularly to the last tie-line found. The set of tie-line extremities forms the binodal. This algorithm is prone to pitfalls such as local optima and three-phase separation; to avoid these, we used a more robust but less accurate method to first visualise the region of instability. Namely, we computed the lower convex envelope of the free energy surface, since it is flat in i directions when coexistence is between $(i + 1)$ phases, $i \in \{1, 2\}$. We are grateful to Peiwen Ren (see Ren, 2023) for his advice and example code performing this computation. Finally, the mean-field percolation transition is obtained by solving an appropriate Flory–Stockmayer condition (Dobrynin, 2004, eq. 17; Santra et al., 2021, fig. 18a)

$$p - q = \frac{1}{(1 - q)s - 1} \quad (14)$$

for the sticker conversion p as a function of the vitrimer fraction ϕ , with $q = q(p, \phi)$ from eq. (6).

Figure 3 shows the resulting phase diagram, for parameter values chosen to match the simulations performed in section 3. We note that instability tends to set in as cross-links are added to the system, globally raising p . Generically, the system separates into ‘sol’ and ‘gel’ phases, as the percolation transition passes very near to the plait point. As p increases, these two phases increasingly share the same local p value.

Qualitatively, our phase diagram is similar to those of Dobrynin (2004) and Semenov and Rubinstein (1998). Heuristically, the globally conserved sticker conversion (p) in associative networks can be compared to the attractive volume of a bond (λ , which depends exponentially on the energy of association) in dissociative networks: both control the density of the resulting network, and for the purposes of visualisation can be plotted as the ordinate of the phase diagram against the vitrimer concentration variable on the abscissa. Doing so, we observe the same topological features, namely two-phase regions for high p (resp. λ) often – but not always – separating between a sol and a gel phase. Of course, the difference in control parameters between associative and dissociative polymer networks means that the correspondence is imperfect, and predictions can only ever be compared qualitatively.

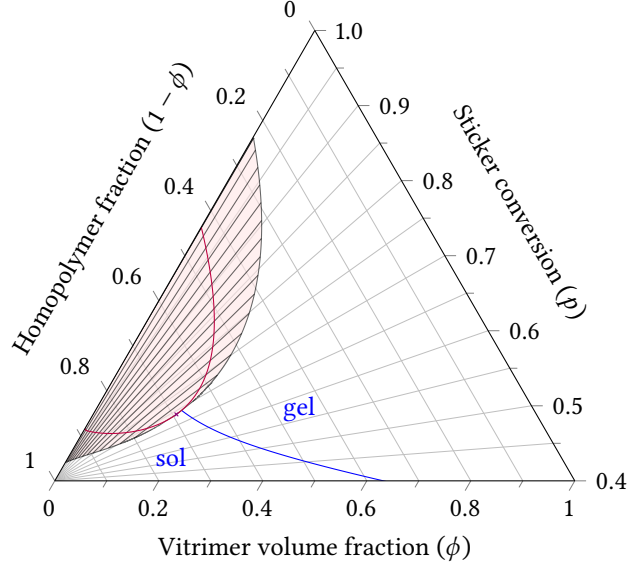


Figure 3: Phase diagram obtained from eq. (5) with $M = N = 20$, $s = 5$ and $k = 0.48$, showing the gelation transition, binodal, spinodal, tie-lines and plait point. *Data are plotted on ‘pinched axes’ as the phase space is naturally triangular. On these axes, lines of constant p are rays emanating from the left-hand corner, whereas lines of constant ϕ connect a value on the vitrimer axis with its complement on the homopolymer axis. Note that we show only a subspace $p \geq 0.4$.*

3 Simulation methodology

To validate the theoretical framework proposed in section 2, molecular dynamics simulations were performed to investigate phase separation phenomena in purely entropic vitrimer-homopolymer blends. We employ the widely adopted coarse-grained Kremer-Grest bead-spring model (Kremer and Grest, 1990) utilising fully flexible chains without angular potentials. A system of 2000 chains, each of length $N = 20$ beads, were initialised in a cubic periodic box with size $L \gg 5 R_g$ (where R_g is the mean radius of gyration), such that the monomer number density was $\rho = 0.85 \sigma^{-3}$. The vitrimer volume fraction ϕ was varied in the interval $\phi \in [0.1, 0.9]$, in steps of 0.1. Vitrimer chains are distinguished from homopolymers by the inclusion of evenly distributed monofunctional associative groups (stickers) along the backbone. Specifically, each vitrimer chain contains five stickers, which are distributed along the twenty-bead backbone at positions 2, 6, 10, 14, and 18. A functionalisation of five stickers per chain ensures the system resides well above the percolation threshold (given sufficiently large sticker conversion is achieved), thereby minimising possible topological defects. Furthermore, it allows reasonable computation times.

3.1 Equilibrium molecular dynamics

Excluded volume interactions between non-bonded beads are modelled by the purely repulsive Weeks–Chandler–Andersen (WCA) potential (Weeks et al., 1971), a Lennard-Jones (LJ) potential truncated and shifted at $r_c = 2^{1/6} \sigma$:

$$U_{\text{LJ}}(r) = \begin{cases} 4\epsilon \left[\left(\frac{\sigma}{r}\right)^{12} - \left(\frac{\sigma}{r}\right)^6 \right] + \epsilon & \text{for } r \leq r_c \\ 0 & \text{for } r > r_c \end{cases} \quad (15)$$

where r denotes the inter-particle distance, while ϵ and σ represent the fundamental energy and length scales respectively. The simulations employ standard reduced units with bead mass m_0 and Boltzmann constant k_B . Consequently, time is expressed in units of $\tau := \sigma (m_0/\epsilon)^{1/2}$.

Connectivity between adjacent backbone monomers, as well as the reversible cross-links formed between stickers, is governed by a finitely extensible non-linear elastic (FENE) potential (Kremer and Grest, 1990). This potential superposes the attractive entropic spring with the purely repulsive WCA component to prevent ‘bond crossing’ (*i. e.*, bonds passing through each other), thus respecting topological constraints:

$$U_{\text{FENE}}(r) = \begin{cases} -\frac{1}{2}KR_0^2 \log \left[1 - \left(\frac{r}{R_0}\right)^2 \right] + U_{\text{LJ}}(r) & \text{for } r < R_0 \\ \infty & \text{for } r \geq R_0 \end{cases} \quad (16)$$

where $K = 30 \epsilon/\sigma^2$ is the spring constant and $R_0 = 1.5 \sigma$ represents the maximum bond length.

Prior to the activation of reversible cross-linking, the polymer melt underwent a multi-stage equilibration protocol maintained at a reduced temperature $T^* = 1 \epsilon/k_B$ using a Langevin thermostat ($\tau_{\text{damp}} = 0.1 \tau$). To eliminate initial steric overlaps and thermally equilibrate the system, non-bonded interactions were initially governed by a soft repulsive potential. This relaxation phase proceeded for a total of 2×10^8 time steps, beginning with an integration step of $\delta t = 0.001 \tau$ which was subsequently increased to $\delta t = 0.005 \tau$ to accelerate relaxation. Following the removal of high-energy overlaps, the standard Lennard-Jones potential of eq. (15) was restored, and the system was equilibrated for a further 10^8 time steps with $\delta t = 0.001 \tau$.

To closely control sticker conversion, we developed a controlled cross-linking procedure. Every 10 time steps, unreacted stickers were allowed to form a maximum of 1 bond with another sticker using the `fix bond/create` command available in LAMMPS (Thompson et al., 2022). The capture radius was set to $R_{\text{min}} = 1.4 \sigma$ to restrict bonding to the first coordination shell, and prevent high energy bonds from forming near R_0 . Secondly, the probability of creating a bond between two candidate stickers was set to $P_{\text{bond}} = 0.0001$ to allow the gradual build-up of cross-linking density. Sticker conversion (p) was monitored using an external Python script; as soon as the desired cross-linking density was achieved, bond creation was turned off and the mixture was equilibrated in a canonical (NVT) ensemble with time step $\delta t = 0.01 \tau$ for a total of 10^8 time steps. The bond potential of the formed cross-links is described by eq. (16). At this stage, all cross-links between stickers were permanent in nature.

Following equilibration and cross-linking, dynamic bond exchange reactions were activated. These measurement runs were conducted in a canonical ensemble, where temperature was maintained at $T^* = 1 \epsilon/k_B$ using a Langevin thermostat ($\tau_{\text{damp}} = 0.5 \tau$). Newton’s equations of

motion were integrated with a time step of $\delta t = 0.01 \tau$ for a total duration of 10^8 time steps. Every 10^3 time steps, bond exchange reactions were allowed to occur using the algorithm described in section 3.2. Initiating data collection immediately upon the activation of bond exchanges allowed us to monitor the phase separation kinetics in real time, capturing the system’s evolution from the precise moment topological reconfigurations began.

3.2 Bond exchange reactions

Vitrimers are classified as associative covalently adaptive networks (asso-CANs) (Denissen et al., 2016). A defining characteristic of this class of material is the strict conservation of cross-link number, maintained through an exchange mechanism where bond cleavage is immediately followed by bond formation (Ricarte et al., 2019). To capture this topology-altering behaviour in the melt state, hybrid Monte-Carlo / molecular dynamics (MC/MD) algorithms have been used extensively (Cui et al., 2023; Perego and Khabaz, 2020, 2021; Perego, Lazarenko et al., 2022; Xia et al., 2023). Building upon the framework established by Cui et al. (2023), we extended their MC/MD algorithm to explicitly incorporate exchange reactions involving non-bonded, ‘free’ stickers.

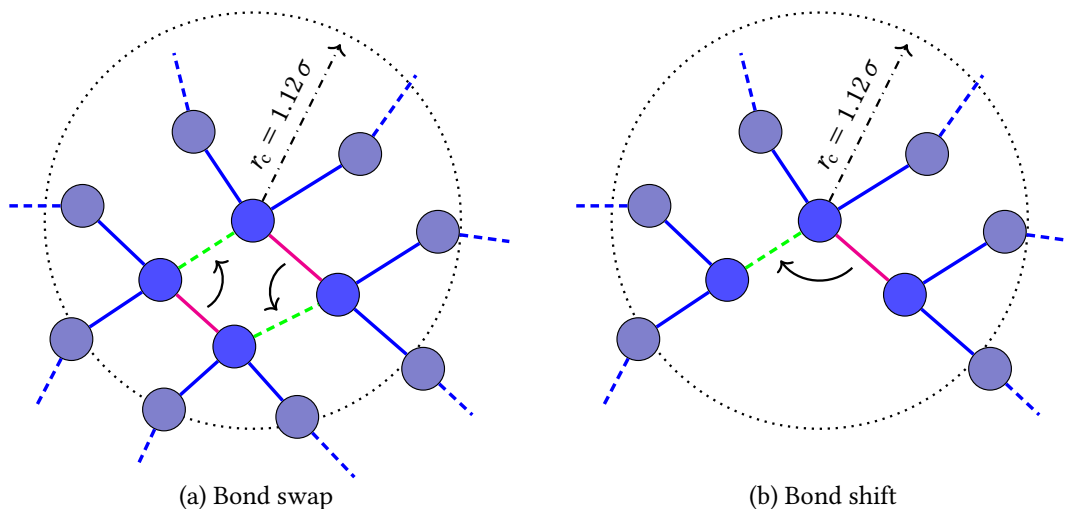


Figure 4: Bond exchange reactions (BER).

Bond exchange can occur through two distinct reaction pathways. A ‘bond swap’ (fig. 4a) involves the metathesis between two existing cross-linked sticker pairs, whereas a ‘bond shift’ (fig. 4b) is facilitated by the presence of a free sticker in the immediate vicinity of a bonded pair. Crucially, both reaction types are subject to a strict proximity criterion, requiring all participating stickers to be within a defined cut-off radius $r_c = 1.12 \sigma$. This cut-off value corresponds to the minimum of the WCA potential ($2^{1/6} \sigma$), representing the direct contact distance between non-bonded stickers. This strict spatial constraint for bond exchange attempts serves two purposes: first, it mimics the steric requirements of an associative reaction mechanism, ensuring the new bonding partner is in the immediate coordination shell; second, it ensures that newly

formed cross-links are created near their equilibrium length ($\approx 0.96 \sigma$), minimising high-energy stretched states and eliminating the possibility of bond crossing upon formation of new cross-links. Consequently, the local spatial distribution of stickers dictates the eligibility of specific sites for exchange events.

For each possible proposed move, the change in potential energy is calculated as:

$$\Delta U = \sum U_{\text{FENE}}^{\text{new}}(r) - \sum U_{\text{FENE}}^{\text{old}}(r) \quad (17)$$

where $\sum U_{\text{FENE}}^{\text{new}}(r)$ and $\sum U_{\text{FENE}}^{\text{old}}(r)$ are the cumulative FENE potentials of the newly proposed (post-exchange) and the original (pre-exchange) bonds, respectively. For both reaction pathways depicted in fig. 4, two distinct new configurations are possible. Candidates were screened by energy minimisation: namely, we retained only the configuration with the lowest ΔU .

The acceptance of the proposed bond exchange reaction (BER) is then governed by the standard Metropolis criterion (Metropolis et al., 1953). Moves resulting in a net reduction of potential energy ($\Delta U \leq 0$) are accepted unconditionally, whereas energetically unfavourable ($\Delta U > 0$) BERs are only accepted with an exchange probability

$$P_{\text{acc}} = \exp\left(-\frac{\Delta U}{k_{\text{B}}T^*}\right). \quad (18)$$

To eliminate the possibility of bond exchange reversals within a given integration cycle, stickers that have participated in a successful exchange are excluded from further bond exchange attempts during that cycle. This means that each sticker is limited to a maximum of one bond topological change per MC step.

Strict detailed balance is violated in the algorithm due to the sequential processing of bond exchange candidates, as the exclusion of reacted stickers from subsequent moves within the same time step introduces a non-Markovian dependency on the random iteration order. Nonetheless, the bond exchange reaction algorithm does satisfy the weaker criterion of global balance, which is the necessary and sufficient requirement for Monte-Carlo simulations (Manousiouthakis and Deem, 1999). On the other hand, when screening the two proposed configurations by energy minimisation, a deterministic choice is introduced which technically violates the balances.

Since the difference in potential energy between the two candidates is generally a multiplicative factor, the higher energy candidate would have an acceptance probability several orders of magnitude smaller due to the exponential suppression in eq. (18). Therefore, the error introduced by this choice is negligible, and it has the benefit of allowing a significant speed-up in the Monte Carlo algorithm. Thus, this preference towards lower energy transitions identifies dominant reaction pathways, effectively filtering out statistically negligible high-energy transitions. This is applicable for the temperatures generally used in Kremer–Grest simulations ($T^* \lesssim 2 \epsilon/k_{\text{B}}$).

3.3 Inferring stability

In simulations, it is possible to observe the development of phase separation over time. Starting from an equilibrated, permanently cross-linked network, BERs are turned on and the measurement run starts. The state of the system is inferred at regular time intervals by recording

atom coordinates and measuring the distribution and local concentration of beads belonging to vitrimeric chains (both ordinary beads and stickers).

Local properties are calculated by discretising the simulation box into $7^3 = 343$ equal-volume subdomains. To mitigate bias arising from arbitrary boundary placement, the discretisation grid was shifted incrementally along all three axes in steps of one-tenth the subdomain side length. These choices – dividing each side of the simulation box into seven equally sized segments and performing ten grid shifts in each dimension – were guided by two considerations. First, both numbers are coprime, ensuring that no two sampled configurations are identical. Second, splitting the simulation box into seven equal segments along each axis yields a subdomain length of approximately 5σ , which is large enough to contain a sufficient number of beads to average over, while remaining small enough to produce observable differences between subdomains. Taking into consideration the periodic boundary conditions, this generates an ensemble of 343 000 subdomains. Here, we describe three distinct methods of determining stability from these discretised subdomains.

Distribution plots

The simplest way to infer the stability of a system is by looking at the number distributions of vitrimeric beads in the (equally sized) subdomains. Stable systems exhibit the expected Gaussian-like distribution, whereas for unstable systems, a split in the distribution is observed, indicative of two distinct phases forming within the melt.

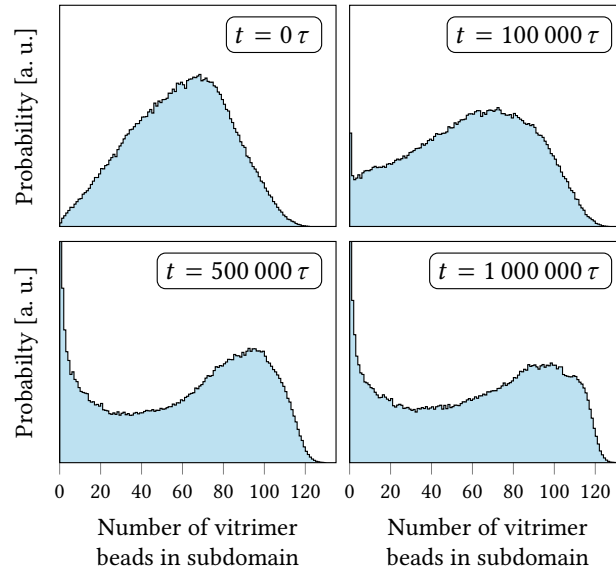


Figure 5: Atom count distribution of vitrimeric beads at four different times during simulation ($\phi = 0.5$, $p = 0.95$). The entire simulation lasted a total of $t = 10^6 \tau$, or 10^8 time steps.

The development of these distributions over time (fig. 5) can give information regarding the rate at which phase separation is developed and when equilibrium is reached. Results reveal that equilibration is invariably reached by the half-way point of the entire simulation (10^8 time steps), with only slight, stochastic deviations observed afterwards.

Distribution plots prove useful to determine phase separation for well separated systems, where both phases occupy reasonable fractions of the simulation box. For such systems, the distribution plots show clear bimodal distributions. However, for ‘edge’ cases where bimodality is not apparent, more advanced tools are needed to quantitatively determine phase separation. For this purpose, two alternative methods to infer stability are presented, based on the spatial correlation function and on density variance, respectively.

Spatial correlation

The stability of the systems were primarily determined from the spatial correlation function. First, we calculate the local composition $\phi(i)$ of the i^{th} subdomain, defined as the proportion of beads in the subdomain that belong to vitrimer chains. This is then correlated with that of all other subdomains as a function of their centre-to-centre Euclidean distance r according to the formula $\sum_{ij} [\phi(i) - \phi][\phi(j) - \phi]$, where ϕ is the global average composition and the sum is taken over all subdomain pairs (i, j) separated by a fixed distance r . An example of this correlation is shown in fig. 6 for $\phi = 0.5$.

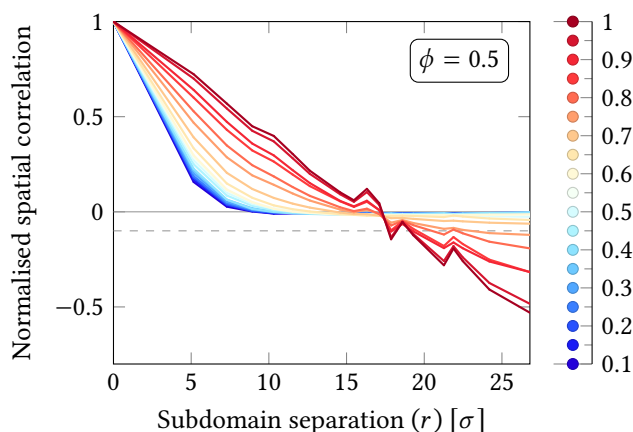


Figure 6: Spatial correlation, for $\phi = 0.5$ and different sticker conversions p , as a function of the distance between subdomain centres. The cut-off point for determining stability is indicated by the horizontal dashed line. The same plots for other values of ϕ can be found in the supplementary information (appendix D).

Formally, for a macroscopic system, phase separation would correspond to an infinite correlation length appearing in the system. Non-phase-separated systems would then have a spatial correlation function that decays to zero over a finite distance. Unfortunately our simulations are necessarily finite, with a simulation box made even smaller by its periodic boundaries. This means that: (i) the largest correlation length available corresponds to about

half the diagonal of the simulation box, *i. e.* about 30σ ; (ii) a phase-separated system will have strong positive correlations in composition up to around half the simulation box size, and negative correlations at large distances because of the overall mass conservation in the finite box; but (iii) such negative correlations are also observed as we approach the region of instability in parameter space, because the diverging correlation length quickly approaches the simulation box size. As a result, it is difficult to distinguish the exact point at which phase separation occurs in a finite simulation box: for intermediate cases it may be impossible to decide between a system with long correlations near the phase-separated state, and a system that is actually phase separated. Hence, plotting the spatial distribution function for different values of p gives a continuum of curves rather than a discontinuous change at phase separation. As a practical choice, we decided to take an anticorrelation of -0.1 at large distances as a heuristic criterion for phase separation. It should be noted that this value is most likely size-dependent and may require adjustment for different box volumes. As can be seen from fig. 6, this criterion also corresponds roughly to the point where the zero of the spatial correlation function approaches that found for the clearly phase separated systems (at larger p).

Density variance

To support the conclusions drawn from the spatial correlation on the stability of a system, we also look at the change in density variance over time. It is defined as $\sigma_\rho(t)^2 = \langle \rho_i(t)^2 \rangle - \langle \rho_i(t) \rangle^2$, where $\rho_i(t)$ is the vitrimer bead density for each subdomain i at time t , and $\langle \cdot \rangle$ is the average over subdomains. When normalised by the density variance at $t = 0$ (the moment before which only permanent cross-links existed between stickers), stable and unstable configurations show opposing behaviour.

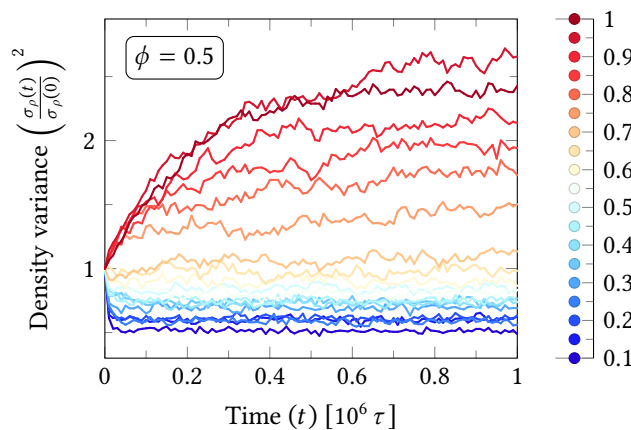


Figure 7: Density variance as a function of time for $\phi = 0.5$ at different sticker conversions p . The same plots for other values of ϕ can be found in the supplementary information (appendix D).

Figure 7 shows the density variance as a function of time for systems with $\phi = 0.5$. The different lines correspond to different sticker conversions (p). Systems that phase separate

show an increase in their normalised density variance over time, until a stable plateau is reached halfway through the simulation. An increase in density variance is indicative of melt heterogeneity (phase separation). Conversely, stable blends show a decrease in variance, synonymous with increased homogeneity and therefore stability. We classify systems into three categories according to the value of their density variance at large times: less than 1, stable; between 1 and 1.5, ambiguous; above 1.5, unstable. We note, as we did for spatial correlation, that these thresholds may change depending on the volume of the simulation box.

When looking at fig. 7 a question arises: why does the density variance for stable systems decrease relative to the starting state? This phenomenon can be attributed to the increased mobility induced by BERs. By turning on BERs, the system is able to equilibrate further than it was previously capable to with permanent cross-links, and the increased mobility of beads permits a more homogeneous state. This argument supports the idea that an increase in density variance can be attributed to phase separation.

3.4 Percolation transition

It is also important to conceptually validate the Flory–Stockmayer prediction of the gelation line. Gelation is defined as the first point at which an infinitely large network forms, spanning the entirety of the sample. In MD simulations, this is the moment at which the probability of finding a cluster spanning the entire simulation box becomes non-zero by forming an ‘infinite’ network through the periodic boundaries.

We follow the method developed by Livraghi et al. (2021) to determine the percolation threshold from MD simulations and compare it to the prediction given by eq. (14). Their estimate threshold is defined by the reduced molecular weight (RMW) and point of inflection of the largest-mass cluster. The RMW is defined as the molecular weight average of all clusters in the system except the largest one. The largest cluster’s size is a more indirect measurement of gelation, where the moment at which the mass of the largest cluster starts to significantly outweigh the other clusters is used as the gelation point. Here, we use both methods to get the most reliable estimate of the critical sticker conversion (p) needed to achieve gelation. The use of both methods is justified considering that the values of p were varied in steps of 0.05, which may be too low of a resolution for an exact match between theory and simulations.

Figure 8 demonstrates the two methods described above for the estimation of the gel point at a vitrimer fraction $\phi = 0.5$. The result obtained from the maximum of the RMW curve predicts a lower critical value for the onset of percolation, $p = 0.4$. On the other hand, the inflection point of the largest cluster size estimates a higher onset ($p = 0.475$). Using these two methods of determining the sol–gel transition, we can provide a confidence interval for percolation in the simulated systems. This result can then be compared to the prediction given by the mean-field theory in eq. (14).

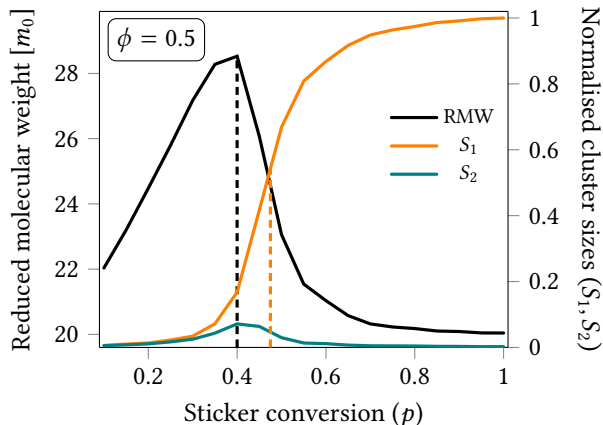


Figure 8: Percolation transition measurements for $\phi = 0.5$. *Black curve: reduced molecular weight (RMW); orange curve: normalised largest cluster size (S_1); teal curve: normalised second largest cluster size (S_2).* Dashed lines indicate the maximum of the RMW and the inflection point of S_1 . The same plots for other values of ϕ can be found in the supplementary information (appendix D).

4 Results and discussion

4.1 Comparison between theory and simulations

We are finally ready to compare the theoretical phase-diagram predictions with the results of simulations. We initialise the free energy with parameter values dictated by the simulations: choosing a discretisation such that every bead fills exactly one lattice site, the parameters $M = N = 20$ and $s = 5$ are straightforward from section 3. The free parameter k was estimated by visually fitting to the simulation results, and found to be somewhere around one half: $k = 0.48 \pm 0.08$. (This motivated the earlier choice of values in fig. 3.) For better visibility of the simulated data, we refrain from using ‘pinched axes’ in favour of a more traditional square plot, giving fig. 9. Note that on square axes, tie-lines are *not* straight line segments, and thus are not shown. On the same plot, we show the spinodal curve (red line, inside the region of instability), and the mean-field percolation transition (blue line).

The results of simulations are split into three classes – stable, clearly phase separated, and borderline – and shown on fig. 9 using symbols. The confidence interval for the percolation transition, obtained using the methods in section 3.4, is indicated by a pale blue region. The region forms a band around the theoretical prediction for $\phi \geq 0.5$, when the mean-field theory is expected to be most accurate; the agreement is worse for smaller values of ϕ , when same-chain bonds become important and the mean-field assumptions weaken.

Looking at the distribution of simulation results, we see that all systems which displayed clear phase separation in the simulations lie within the theoretical region of instability. There is some uncertainty near the boundary, due to the gradual onset of separation in simulations as the p -value increases (as discussed in section 3.3). Nonetheless, we find very good agreement between theory and simulations at an appropriately chosen value for the free parameter k .

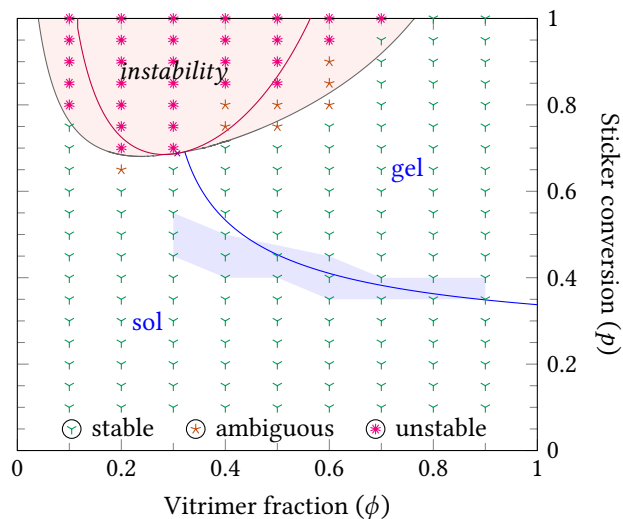


Figure 9: Phase diagram from theory (lines) and from simulations (symbols). *Three classes of stability are shown: stable, clearly phase separated, and ambiguous or borderline. The free-energy parameters are $M = N = 20$, $s = 5$, and $k = 0.48$. This figure shows the same theoretical data as fig. 3, plotted on square axes to maximise visibility of the simulation points for small ϕ . The percolation transition seen in simulations (section 3.4) appears as a pale blue band.*

4.2 Consistency of the local-bonding parameter

How reasonable is this fitted value $k \approx 0.48$? We can check consistency by calculating it in different ways. One is to use the result for Gaussian chains, eq. (11), applied to a lattice based on the MC/MD beads. Here, the bond length is around the minimum of the FENE potential ($b \approx 0.96 \sigma$); every bead is a statistical segment, so the Kuhn volume is that of a bead ($v_K = \frac{\pi}{6} \sigma^3$); and every lattice site corresponds to one bead ($v_0 = v_K$). Using these values in eq. (11) gives $k \approx 0.39$, in agreement with the fitted uncertainty 0.48 ± 0.08 .

Whilst the accuracy of this agreement is to some extent coincidental – for example, if instead of using as unit volume the size of a bead ($v_0 = v_K$) we had used the inverse number density of monomers in the simulation box ($v_0 = 1/\rho \approx 1.18 \sigma^3$), the estimate would have risen to $k \approx 0.88$ – it remains heartening to find a result of the correct order of magnitude. This can be compared with another way to verify consistency, namely measuring the values of p and q directly in the simulations and using them to solve for k in eq. (6). Limiting this analysis to systems which unequivocally do *not* undergo phase separation, we obtain $k \approx 0.20$ from the fraction of cross-links which are between nearest-neighbour stickers on the same chain. Note however that this is expected to be an underestimate: in the simulated systems, same-chain bonds are not limited to being between nearest-neighbour stickers, and can span the whole chain; nearest-neighbour bonds are thus less likely than they might be in a nearest-neighbour-only system. To compensate for this, we can imagine a different definition of q in simulations: instead of using the fraction of bonds which are between *nearest-neighbour* stickers, we can

measure the fraction of bonds which are between *any two stickers on the same chain*. Using this alternative definition for q in eq. (6) gives $k \approx 0.30$ on average. (Figure 10 shows the detail of the calculation for both q variants, plotting the equivalent k value for each simulated sticker conversion p and vitrimer volume fraction ϕ .) For stable systems, the predicted values of k remain approximately constant, and the value starts to drop as soon as instability sets in, since the single-phase percolation condition ceases to apply. As with the previous method, we find a value of the correct order of magnitude, though the estimate is now further from the fitted value.

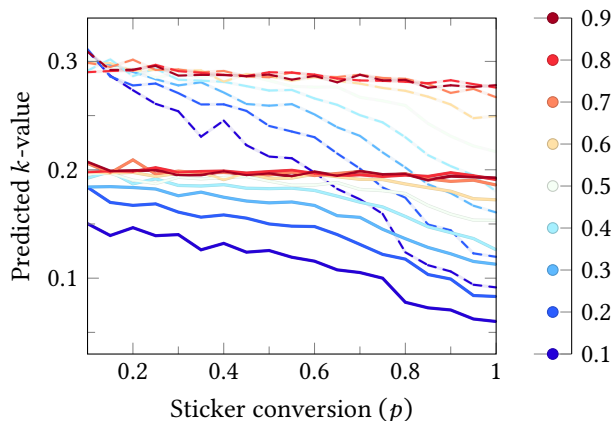


Figure 10: Value of the left-hand side of eq. (6) as a function of p for all values of ϕ . *Solid lines indicate calculations involving only nearest-neighbour cross-links, dashed lines correspond to calculations involving all same-chain cross-links.*

A third method of controlling consistency is to return to the definition $k := \mathbb{P}[l_{N/s}] \times 4N/(sx)$. Assuming beads in the simulation are to a good approximation hexagonally packed, each sticker has roughly $x = 12 - 2 = 10$ free sites adjacent to it. The natural discretisation – one bead per lattice volume – makes N/s the number of bead diameters between successive stickers. The only missing quantity is then $\mathbb{P}[l_{N/s}]$, the probability that two nearest-neighbour stickers are within a bond length of each other. This quantity can be obtained from the simulations by observing a system sure not to separate – *e. g.*, $\phi = 0.9$ and $p = 0.5$ – and counting, amongst all nearest-neighbour sticker pairs, which proportion are less than a distance $2 \times 0.96 \sigma$ apart. (In fact, to avoid interference from the cross-linking algorithms, we look only at beads on *homopolymer* chains spaced four bond lengths apart.) We find a probability $\mathbb{P}[l_4] \approx 0.3$, yielding a value $k = 0.48$.

4.3 Phase diagram for a realistic blend

Comparison with simulations suggests good reason to be confident in the applicability of the theoretical model. In this section, we provide a phase diagram for a more realistic choice of parameters, inspired by a polystyrene-based vitrimer chemistry.

Steric cross-linker and stopper

Thus far, we have approximated cross-linker and stopper moieties as ‘phantom’ objects, occupying no volume. Depending on the size of these two moieties, however, the approximation may have limited applicability. To relax this assumption, we split the vitrimer network into three types of component: the chain backbone (B), the cross-linker (C) and the stopper (D). Each component – or, for simplicity, ‘species’ – is considered to occupy a volume N_i in discretisation units: the index i runs over the four species in our system, the remaining species (A) being the homopolymer chains. This gives four volume fractions ϕ_i of which to keep track.

Repeating the argument in section 2 for a four-species system gives an intensive free energy

$$f = -\mathfrak{H} \left(\frac{s\phi_B}{N_B} - \frac{q}{p} \frac{\phi_C}{N_C} \right) + \sum_i \frac{\mathfrak{H}(\phi_i)}{N_i} + \left[\mathfrak{H}(1 - q/p) + \mathfrak{H}(q/p) + \frac{q}{p} \log \left(\frac{2N_B}{esk} \right) \right] \frac{\phi_C}{N_C}, \quad (19)$$

with $q \approx kp/(k + 2\phi_B)$, where the four volume fractions ϕ_i are related by the stoichiometric condition $s\phi_B/N_B = 2\phi_C/N_C + \phi_D/N_D$ and the – obvious – new volume balance, $\sum_i \phi_i = 1$. The degree of conversion is also updated, to $p = 2N_B\phi_C/(sN_C\phi_B)$. In the interest of brevity, the derivation of these results is relegated to the supplementary information (appendix A.3).

The consistency of eq. (19) with the expressions in sections 2 and 3 can be seen by relabelling $N_A = M$ and $N_B = N$; setting $\phi_C = (sN_C/2N_B)\psi$ and $\phi_D = (sN_D/N_B)(\phi - \psi)$; and finally, taking the volume balance $\sum_i \phi_i = 1$ in the limit of small cross-linker and stopper size ($sN_C \sim sN_D \ll N_B$) to claim that $\phi_B = \phi = 1 - \phi_A$. It can be verified that the result of this procedure is the simplified system discussed up to now.

Figure 1b showed the chemical structure of a polystyrene vitrimer–homopolymer melt, categorised into our four species A, B, C and D (based on dioxaborolane functional groups). The cutting-point between B and C/D is chosen to be the point where the chemical bonds break during a cross-link exchange interaction. For such a system, what values should be used for the parameters N_i , $i \in \{A, \dots, D\}$? Recall that the on-lattice parameters N_i are defined as the number of lattice sites occupied by a single representative of a given species. As such, they are equal to the volume occupied by that representative divided by the unit lattice-site volume: $N_i = v_i/v_0$. Therefore, it suffices to estimate the volume of one representative from each species, since the free energy is invariant under rescaling of the elementary lattice volume v_0 .

Given degrees of polymerisation dp_A and dp_B and vitrimer functionality s , the volume occupied by each species can be approximated by its mass. Counting atoms in fig. 1b gives

$$\begin{aligned} N_A &= dp_A & N_B &= dp_B + \frac{47}{52}s \\ N_C &= 5/4 & N_D &= 1 \end{aligned} \quad (20)$$

where the parameters N_i are generated by scaling every mass by the same factor of 104 Da.

Longer chains

The degrees of polymerisation used for simulations – twenty beads, five stickers – are constrained by the numerical capacity of the computers at our disposal. In real applications, we

might expect chains to have monomer counts somewhere in the thousands, and function sites numbering hundreds. We thus take our new-found, fully steric expressions and apply them to a system with chains orders of magnitude longer.

As a plausible example, we consider both homopolymer and vitrimer to have degree of polymerisation $dp_i = 1500$ and assume $s = 200$ stickers per vitrimer chain (corresponding to a molecular weight of 175 kDa for the vitrimer and 156 kDa for the polymer). For the unknown parameter k , we recall the scaling law in eq. (11) and arbitrarily set $k = (s/N_B)^{1/2} \approx 0.34$. This is consistent – recall eq. (8) – with values for the packing length ($P \approx 4 \text{ \AA}$) and root-mean-square end-to-end distance ($R_s \approx 20 \text{ \AA}$) experimentally measured for polystyrene (Fetters et al., 1999; Unidad et al., 2015).

Figure 11 shows the resulting phase diagram. (Due to lack of convergence of the numerical method in the immediate neighbourhood of the plait point, the binodal in that region is interpolated between the plait points and the first tie-lines identified.) The most striking feature is the onset of instability, which now occurs at much lower values of p .

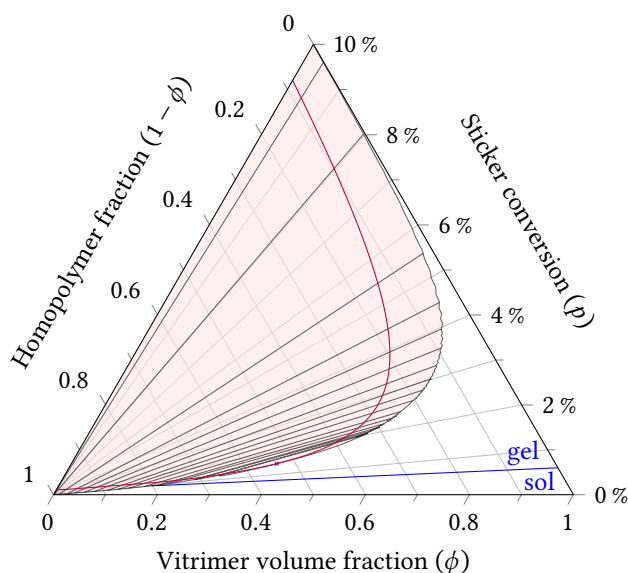


Figure 11: Phase diagram for a hypothetical polystyrene-based vitrimer melt. *Parameter values are $dp_A = dp_B = 1500$, $s = 200$ and $k \approx 0.34$. Since the p -axis starts at zero, horizontal sections of this plot correspond to slices of constant ψ .*

This last statement can be made more precise by solving for the plait point in the simplest available model when chains do not bond to themselves ($k = 0$). This is equivalent to solving eqs. (12) and (13) for the free energy given in eq. (3), with $N = M$. Doing so in a computer algebra system provides an exact solution for the plait point, which can be asymptotically expanded to first order in $1/s$, yielding

$$\begin{aligned} \phi &= \frac{1}{2} - \frac{3}{2s} + \mathcal{O}(s^{-2}) \quad \text{and} \quad \psi = \frac{1}{s} + \mathcal{O}(s^{-2}) \\ \implies p &= \frac{2}{s} + \mathcal{O}(s^{-2}) . \end{aligned} \quad (21)$$

Whilst the correct estimate for the plait point is heavily dependent on the value of k , eq. (21) gives a rule of thumb for the onset of instability: the larger the number of stickers on the vitrimer chains, the smaller the critical p value for instability, roughly in reciprocal relation. We emphasise this particular result, as it is helpful in guiding experimental exploration of the design space of vitrimer–polymer blends.

The scaling $p \sim 1/s$ in eq. (21) can even be used to provide a similar rule of thumb for the case with nearest-neighbour bonds ($k > 0$), through a bootstrap-like argument. Repeating the preceding analysis with the corrected free energy of eq. (5), but setting $p = p_0/s$ and having the computer algebra system take eqs. (12) and (13) in the limit $s \rightarrow \infty$ gives the solution $p_0 = 2 + 2k$, or equivalently

$$p \approx \frac{2}{s} (1 + k) \quad (22)$$

to first order. Here, the average spacing of stickers along the backbone makes an appearance through the dependence on k , which by eqs. (8) and (11) scales as $k \sim P/R_s \sim \sqrt{s/dp_B}$. Increasing the density of stickers along the vitrimer chain whilst keeping the functionality constant is thus expected to displace the onset of instability towards higher degrees of conversion.

4.4 Limitations of the model

Certainly the primary limitation of the model presented is its pure-entropic nature. In a real system, configurations have enthalpy: due to the interaction between atomic potentials; due to compressibility of the sample; due to the effect of temperature; – none of this is accounted for in our model. Of these, the energetic interactions of adjacent atoms are a particularly important omission. In the simplest case of a melt of identical backbone chemistries, as the proportion of monomers which are functions (s/dp_B) grows small, we expect the effect of energetic interactions to scale with the number of contacts between homopolymer and vitrimer backbone on one side, and cross-linker and stopper moieties on the other. Using the interaction parameter χ of Flory–Huggins solution theory, this scale is roughly $\chi s/N_B$. The energetic term will affect the position of the binodal line when it is comparable to the stable, Flory–Huggins term of the free energy, which scales as $\max\{N_A^{-1}, N_B^{-1}\}$. For equal chain lengths $N_A = N_B$, this suggests that the relevant parameter for energetic effects in our networks is χs , which is much less than the relevant parameter in homopolymeric melts χN_B . We thus expect energetic effects to be suppressed in vitrimeric melts.

Another limitation is the model’s treatment of the weakly concentrated regime ($\phi \ll 1$). In the presence of an energetic interaction with the solvent/matrix, previous literature has suggested that the vitrimer chains would form globular structures (Dobrynin, 2004; Semenov and Rubinstein, 1998). We believe this mechanism to be absent in the entropic formalism presented in this paper. Nonetheless, a significant aspect of the entropic case has been neglected in our treatment: namely, the higher-order ‘harmonics’ of same-chain cross-linking, which drive chain collapse in real physical systems (Berda et al., 2010). We neglected these under the assumption that they are suppressed by their polynomial entropic cost, their contribution to the partition function scaling as $(\text{loop length})^{-3/2}$. We know from eq. (4) that the number of possible nearest-neighbour-only configurations on s sites with c cross-links is $(s - c)!/[c!(s - 2c)!]$, and from eq. (2) that the total number of configurations on s sites with c cross-links is $s!/[2^c c!(s - 2c)!]$. This means that the proportion of configurations which are nearest-neighbour only is the ratio of the first to the second, or

$$\frac{2^c (s - c)!}{s!} \approx \exp \left[-c \log \left(\frac{s}{2} \right) + \mathcal{O} \left(\frac{c}{s} \right) \right]. \quad (23)$$

This quantity vanishes factorially as s grows large, largely overtaking the suppression factor associated with non-nearest-neighbour cross-links. This leads us to suggest that as the number of functions on a given vitrimer chains grows, the cross-linking behaviour of isolated vitrimer chains is not dominated by that between nearest-neighbour stickers, but exhibits cross-links between stickers of arbitrary separation along the backbone. This combinatorial effect will be compounded by the fact that a sort of ‘economy of scale’ is at play: once the vitrimer chain is already collapsed, longer-range cross-links are no longer so entropically expensive as they would originally have been. The topic of isolated vitrimer chains is still an open question for research to tackle.

Finally, we wish to highlight that the mean-field methods used in this article suffer the drawback that they are not spatially resolved: phases are treated as homogeneous throughout. This means that such a theory cannot be used to make meaningful statements about separation into micro-phases; yet if – *e.g.* – the cross-linker is strongly repelled by the vitrimer backbone, we expect the formation of spatially segregated clusters of cross-linked sites. An accurate treatment of such clusters may require the use of a fully-fledged field theory (such as Vigil et al., 2025), with the added complexity that such theories entail.

5 Conclusion

In this study, we have derived a mean-field model for the free energy of an associative covalent polymer network. From the free energy, quantitative predictions can be made for a wide range of melt compositions and cross-link fractions by using appropriate numerical methods.

The model’s validity is supported by the agreement of molecular dynamics simulations with the phase diagram predicted by the theory. These simulations emulated the dynamics of vitrimer–polymer blends by combining a Kremer–Grest bead-spring model with a bespoke Monte-Carlo bond-exchange algorithm. Instability and percolation were detected by comparing features in the distribution and clustering of vitrimer beads within discrete subdomains of the

simulation box; for instability, the variance in bead density and the spatial correlation of the subdomains' deviation from mean composition proved particularly useful in classifying edge cases. Since the vitrimer and homopolymer analogues were made chemically identical, any instability observed was solely a result of the entropic effect of cross-links between stickers.

We predict phase separation for a range of parameter values, even despite the exclusion of energetic effects. Stated differently: blends of otherwise non-interacting polymeric materials can become immiscible merely through the addition of a cross-linking mechanism. This prediction, though consistent with previous work on dissociative systems (Dobrynin, 2004; Semenov and Rubinstein, 1998), nonetheless has a novel aspect: only in *associative* systems is it possible to wholly disregard energetic mechanisms. The phenomena described herein are entirely entropic, and serve as a warning that affinity at a chemical level is in no way a guarantee that a polymer–vitrimer blend will remain homogeneously distributed.

* * *

Supplementary information

Several additional sections are provided in the supplementary information (at the end of this document). These are:

- (A) a full derivation of the free energy in the case of volume-filling cross-linker and stopper;
- (B) further discussion of the possible effects of energetic interactions in dissociative polymer networks;
- (C) a derivation of the free energy (in the 'phantom' approximation) in the case of arbitrary cross-linker functionality; and
- (D) plots of the spatial correlation, density variance and percolation transition measurement for all values of ϕ (except $\phi = 0.5$, corresponding to figs. 6 to 8 in the text).

In the interest of ensuring the reproducibility of our results, we also provide access to the source code used to generate the data in this paper. See the section on open science on the next page for details.

Declarations

Acknowledgements

We thank Peiwen Ren and Lorenzo Contento for their advice on computing the lower convex envelope of a surface; Nathan van Zee for his cartoon of a vitrimer melt; and our colleagues from the ReBond network for fruitful discussions.

Funding

This project has received funding from the European Union's Horizon 2020 research and innovation programme under the Marie Skłodowska-Curie grant agreement № 101119786.

Open science

Following ReBond's commitment to open science, the code used to generate the data for the figures in this paper is made publicly accessible in the Université catholique de Louvain's dataverse for the ReBond project (Magyari and Rispo Constantinou, 2026).

<https://dataverse.uclouvain.be/dataverse/rebond>

The Monte-Carlo bond-exchange logic has also been made available as an open-source PyPI package installable through `pip` under the name `MC-exchange`. The source code can be found on GitHub (Magyari, 2026).

https://github.com/balintmagyari/MC_exchange

Conflicts of interest

The authors declare no competing financial interest.

AI transparency statement

Generative AI (Google Gemini) was used by B. M. to assist in refining the Python scripts used for data analysis and to edit the manuscript for language and clarity. The authors rigorously reviewed and verified all AI-generated outputs to ensure scientific accuracy and assume full responsibility for the final content.

Author contributions

A. A. Rispo Constantinou theoretical framework, manuscript writing (sections 1, 2, 4 and 5)

B. Magyari simulations, data analysis, manuscript writing (sections 3 and 5)

G. Ianniruberto supervision, guidance, manuscript review and editing

E. van Ruymbeke supervision, guidance, manuscript review and editing

D. J. Read supervision, guidance, manuscript review and editing

Contents

1	Introduction	3
2	Free energy model	6
2.1	Derivation	6
2.2	Nearest-neighbour correction	8
2.3	Local bonding propensity	10
2.4	Phase diagram	11
3	Simulation methodology	13
3.1	Equilibrium molecular dynamics	14
3.2	Bond exchange reactions	15
3.3	Inferring stability	16
3.4	Percolation transition	20
4	Results and discussion	21
4.1	Comparison between theory and simulations	21
4.2	Consistency of the local-bonding parameter	22
4.3	Phase diagram for a realistic blend	23
4.4	Limitations of the model	26
5	Conclusion	27
A	Full free-energy derivation	i
A.1	Network cycles	iii
A.2	Links to the same chain	iv
A.3	Nearest-neighbour correction	iv
B	Energetic interactions	v
B.1	A first look	v
B.2	Splitting the molecules	vi
B.3	Globules and micro-phase segregation	vii
C	Cross-linker of arbitrary functionality	vii
D	Additional plots	ix

List of Figures

1	Anatomy of a melt	3
2	Nearest-neighbour bonds	8
3	Theoretical phase diagram	13
4	Types of bond exchange reaction	15
5	Atom count distribution	17
6	Spatial correlation	18
7	Density variance	19
8	Percolation transition	21
9	Comparison of theory and simulations	22
10	Bonding propensity	23
11	Phase diagram for polystyrene melt	25
I	Effect of an energetic interaction	v
II	Polystyrene/dioxaborolane vitrimer melt	vi
III	Variant segmentation of polystyrene/dioxaborolane vitrimer	vii
IV	Further spatial correlation	x
V	Further density variance	xi
VI	Further percolation transition measurements	xii

List of Tables

1	Terminology conversion	6
---	----------------------------------	---

References

- Behbahani, Alireza F. and Friederike Schmid (Jan. 2025). 'Relaxation dynamics of entangled linear polymer melts via molecular dynamics simulations'. *Macromolecules* 58 (1), pp. 767–786. ISSN: 15205835. DOI: 10.1021/acs.macromol.4c02168.
- Berda, Erik B., E. Johan Foster and E. W. Meijer (9th Feb. 2010). 'Toward controlling folding in synthetic polymers: fabricating and characterizing supramolecular single-chain nanoparticles'. *Macromolecules* 43.3, pp. 1430–1437. ISSN: 0024-9297, 1520-5835. DOI: 10.1021/ma902393h.
- Bobbili, Sai Vineeth and Scott T. Milner (1st Nov. 2021). 'Measuring packing length in simulations for different polymer architectures'. *Journal of Rheology* 65.6, pp. 1245–1253. ISSN: 0148-6055, 1520-8516. DOI: 10.1122/8.0000305.
- Chen, Jiuyu, Erqiang Chen and Shuang Yang (28th Oct. 2025). 'Gelation and phase separation in oppositely charged polyelectrolyte solutions: the formation of quadrupoles'. *Macromolecules* 58.20, pp. 11418–11428. ISSN: 0024-9297. DOI: 10.1021/acs.macromol.5c01198.
- Cui, Xiang, Nuofei Jiang, Jingyu Shao et al. (Feb. 2023). 'Linear and nonlinear viscoelasticities of dissociative and associative covalent adaptable networks: discrepancies and limits'. *Macromolecules* 56.3, pp. 772–784. ISSN: 15205835. DOI: 10.1021/acs.macromol.2c02122.
- Danielsen, Scott P. O., Alexander N. Semenov and Michael Rubinstein (25th July 2023). 'Phase separation and gelation in solutions and blends of heteroassociative polymers'. *Macromolecules* 56.14, pp. 5661–5677. ISSN: 0024-9297, 1520-5835. DOI: 10.1021/acs.macromol.3c00854.
- De Heer Kloots, Martijn H. P., Sybren K. Schoustra, Joshua A. Dijksman and Maarten M. J. Smulders (2023). 'Phase separation in supramolecular and covalent adaptable networks'. *Soft Matter* 19.16, pp. 2857–2877. ISSN: 1744-683X, 1744-6848. DOI: 10.1039/D3SM00047H.
- Denissen, Wim, Johan M. Winne and Filip E. Du Prez (2016). 'Vitrimers: permanent organic networks with glass-like fluidity'. *Chem. Sci.* 7.1, pp. 30–38. ISSN: 2041-6520, 2041-6539. DOI: 10.1039/C5SC02223A.
- Dobrynin, Andrey V. (1st May 2004). 'Phase diagram of solutions of associative polymers'. *Macromolecules* 37.10, pp. 3881–3893. ISSN: 0024-9297. DOI: 10.1021/ma0353686.
- Doi, Masao and Samuel F. Edwards (1988). *The theory of polymer dynamics*. International series of monographs on physics. Oxford: Clarendon Press. 391 pp. ISBN: 978-0-19-852033-7.
- Everaers, Ralf, Hossein Ali Karimi-Varzaneh, Frank Fleck et al. (Mar. 2020). 'Kremer-Grest models for commodity polymer melts: linking theory, experiment, and simulation at the Kuhn scale'. *Macromolecules* 53 (6), pp. 1901–1916. ISSN: 15205835. DOI: 10.1021/acs.macromol.9b02428.
- Fantoni, Riccardo and Kristian K. Müller-Nedebock (29th July 2011). 'Field-theoretical approach to a dense polymer with an ideal binary mixture of clustering centers'. *Physical Review E* 84.1, p. 011808. ISSN: 1539-3755, 1550-2376. DOI: 10.1103/PhysRevE.84.011808.
- Fetters, Lewis J., David J. Lohse and William W. Graessley (15th May 1999). 'Chain dimensions and entanglement spacings in dense macromolecular systems'. *Journal of Polymer Science Part B: Polymer Physics* 37.10, pp. 1023–1033. ISSN: 0887-6266, 1099-0488. DOI: 10.1002/(SICI)1099-0488(19990515)37:10<1023::AID-POLB7>3.0.CO;2-T.
- Flory, Paul J (1953). *Principles of polymer chemistry*. 9th printing 1975. Ithaca: Cornell University Press. ISBN: 0-8014-0134-8.

- Ge, Sirui and Christopher M. Evans (22nd Apr. 2025). ‘Influence of segmental dynamics on bond exchange in imine vitrimers with different polymer backbones and cross-linkers’. *Macromolecules* 58.8, pp. 4043–4058. ISSN: 0024-9297. DOI: 10.1021/acs.macromol.5c00067.
- Grosberg, Alexander Yu. and Alexei R. Khokhlov (1994). *Statistical physics of macromolecules*. Trans. by Yuri A. Atanov. AIP series in polymers and complex materials. New York: AIP Press. 350 pp. ISBN: 978-1-56396-071-0.
- Han, Haiping and Xuecheng Xu (2018). ‘Poly(methyl methacrylate)–epoxy vitrimer composites’. *Journal of Applied Polymer Science* 135.22, p. 46307. ISSN: 1097-4628. DOI: 10.1002/app.46307.
- Hayashi, Mikihiro (Apr. 2025). ‘Understanding vitrimer properties through various aspects of inhomogeneity’. *Polymer Journal* 57.4, pp. 343–355. ISSN: 0032-3896, 1349-0540. DOI: 10.1038/s41428-024-00990-x.
- Joosten, Liliana Miriam Aurelia, Philippe Cassagnau, Eric Drockenmuller and Damien Montarnal (2024). ‘Synthesis, recycling and high-throughput reprocessing of phase-separated vitrimer-thermoplastic blends’. *Advanced Functional Materials* 34.1, p. 2306882. ISSN: 1616-3028. DOI: 10.1002/adfm.202306882.
- Kremer, Kurt and Gary S. Grest (1990). ‘Dynamics of entangled linear polymer melts: a molecular-dynamics simulation’. *The Journal of Chemical Physics* 92.8, pp. 5057–5086. ISSN: 00219606. DOI: 10.1063/1.458541.
- Levin, Oscar (2021). *Discrete mathematics: an open introduction*. 3rd ed. [Open Textbooks]. ISBN: 978-1-7929-0169-0. URL: <https://discrete.openmathbooks.org/dmoi3.html> (visited on 09/03/2026).
- Livraghi, Mattia, Kevin Höllring, Christian R. Wick et al. (12th Oct. 2021). ‘An exact algorithm to detect the percolation transition in molecular dynamics simulations of cross-linking polymer networks’. *Journal of Chemical Theory and Computation* 17.10, pp. 6449–6457. ISSN: 1549-9618. DOI: 10.1021/acs.jctc.1c00423.
- Magyari, Balint (Mar. 2026). *MC-exchange*. Version 1.0.2. URL: https://github.com/balintmagyari/MC_exchange (visited on 10/03/2026).
- Magyari, Balint and Alexandros A. Rispo Constantinou (2026). *Replication data for: Entropic phase separation in polymer–vitrimer melts*. Version 1. Open Data @ UCLouvain. DOI: 10.14428/DVN/AABCVQ.
- Manousiouthakis, Vasilios I. and Michael W. Deem (Feb. 1999). ‘Strict detailed balance is unnecessary in Monte Carlo simulation’. *The Journal of Chemical Physics* 110 (6), pp. 2753–2756. ISSN: 0021-9606. DOI: 10.1063/1.477973.
- Metropolis, Nicholas, Arianna W. Rosenbluth, Marshall N. Rosenbluth et al. (June 1953). ‘Equation of state calculations by fast computing machines’. *The Journal of Chemical Physics* 21 (6), pp. 1087–1092. ISSN: 0021-9606. DOI: 10.1063/1.1699114.
- Montarnal, Damien, Mathieu Capelot, François Tournilhac and Ludwik Leibler (18th Nov. 2011). ‘Silica-like malleable materials from permanent organic networks’. *Science* 334.6058, pp. 965–968. ISSN: 0036-8075, 1095-9203. DOI: 10.1126/science.1212648.

- Perego, Alessandro and Fardin Khabaz (Oct. 2020). ‘Volumetric and rheological properties of vitrimers: a hybrid molecular dynamics and Monte Carlo simulation study’. *Macromolecules* 53.19, pp. 8406–8416. ISSN: 15205835. DOI: 10.1021/acs.macromol.0c01423.
- (Nov. 2021). ‘Effect of bond exchange rate on dynamics and mechanics of vitrimers’. *Journal of Polymer Science* 59.21, pp. 2590–2602. ISSN: 26424169. DOI: 10.1002/pol.20210411.
- Perego, Alessandro, Daria Lazarenko, Michel Cloitre and Fardin Khabaz (Sept. 2022). ‘Microscopic dynamics and viscoelasticity of vitrimers’. *Macromolecules* 55.17, pp. 7605–7613. ISSN: 15205835. DOI: 10.1021/acs.macromol.2c00588.
- Prusty, Debadutta, Victor Pryamitsyn and Monica Olvera de la Cruz (14th Aug. 2018). ‘Thermodynamics of associative polymer blends’. *Macromolecules* 51.15, pp. 5918–5932. ISSN: 0024-9297, 1520-5835. DOI: 10.1021/acs.macromol.8b00661.
- Qin, Jian (12th Mar. 2024). ‘Similarity of polymer packing in melts is dictated by \bar{N} ’. *Macromolecules* 57.5, pp. 1885–1892. DOI: 10.1021/acs.macromol.3c02273.
- Ren, Peiwen (17th Mar. 2023). *Convex hull construction of phase diagrams: a visual introduction*. Peiwen Ren. URL: <https://pwren.me/blog/2023/phase-diagram/> (visited on 24/01/2025).
- Ricarte, Ralm G., François Tournilhac and Ludwik Leibler (22nd Jan. 2019). ‘Phase separation and self-assembly in vitrimers: hierarchical morphology of molten and semicrystalline polyethylene/dioxaborolane maleimide systems’. *Macromolecules* 52.2, pp. 432–443. ISSN: 0024-9297, 1520-5835. DOI: 10.1021/acs.macromol.8b02144.
- Röttger, Max, Trystan Domenech, Rob van der Weegen et al. (7th Apr. 2017). ‘High-performance vitrimers from commodity thermoplastics through dioxaborolane metathesis’. *Science* 356.6333, pp. 62–65. DOI: 10.1126/science.aah5281.
- Santra, Aritra, B. Dünweg and J. Ravi Prakash (1st July 2021). ‘Universal scaling and characterization of gelation in associative polymer solutions’. *Journal of Rheology* 65.4, pp. 549–581. ISSN: 0148-6055, 1520-8516. DOI: 10.1122/8.0000235.
- Semenov, Alexander N. and Michael Rubinstein (1st Feb. 1998). ‘Thermoreversible gelation in solutions of associative polymers. 1. Statics’. *Macromolecules* 31.4, pp. 1373–1385. ISSN: 0024-9297, 1520-5835. DOI: 10.1021/ma970616h.
- Shcherbakova, Nataliya, Vincent Gerbaud and Kevin Roger (13th Sept. 2023). ‘Using the intrinsic geometry of binodal curves to simplify the computation of ternary liquid–liquid phase diagrams’. *Entropy* 25.9, p. 1329. ISSN: 1099-4300. DOI: 10.3390/e25091329.
- Skorik, Yury A., Valentina A. Petrova, Olga V. Okatova et al. (July 2016). ‘Characterization of clusters and unimers in associating solutions of chitosan by dynamic and static light scattering’. *Macromolecular Chemistry and Physics* 217.14, pp. 1636–1644. ISSN: 1022-1352, 1521-3935. DOI: 10.1002/macp.201600146.
- Smallenburg, Frank, Ludwik Leibler and Francesco Sciortino (30th Oct. 2013). ‘Patchy particle model for vitrimers’. *Phys. Rev. Lett.* 111.18, p. 188002. ISSN: 0031-9007, 1079-7114. DOI: 10.1103/PhysRevLett.111.188002.
- Tanaka, Fumihiko (7th Sept. 2022). ‘Comparative study on the models of thermoreversible gelation’. *IJMS* 23.18, p. 10325. ISSN: 1422-0067. DOI: 10.3390/ijms231810325.
- Thompson, Aidan P., H. Metin Aktulga, Richard Berger et al. (2022). ‘LAMMPS — a flexible simulation tool for particle-based materials modeling at the atomic, meso, and continuum

- scales'. *Comp. Phys. Comm.* 271, p. 108171. ISSN: 0010-4655. DOI: 10.1016/j.cpc.2021.108171.
- Tompa, H. (1956). *Polymer solutions*. London: Butterworths Scientific Publications. 325 pp.
- Torres, Nat, Daniel C. Barzycki, Zachary R. Bauer et al. (19th Jan. 2026). 'Immiscible polydimethylsiloxane/polybutadiene vitrimer blends'. *Macromolecules*. ISSN: 0024-9297. DOI: 10.1021/acs.macromol.5c02945.
- Unidad, Herwin Jerome, Mahmoud Abdel Goad, Ana Rita Bras et al. (22nd Sept. 2015). 'Consequences of increasing packing length on the dynamics of polymer melts'. *Macromolecules* 48.18, pp. 6638–6645. ISSN: 0024-9297, 1520-5835. DOI: 10.1021/acs.macromol.5b00341.
- Vigil, Daniel L., Glenn H. Fredrickson and Jian Qin (14th Oct. 2025). 'Coherent state field theory for reversible gelation of star polymers'. *Macromolecules* 58.19, pp. 10920–10936. ISSN: 0024-9297. DOI: 10.1021/acs.macromol.5c01825.
- Wang, Zongtao, Yu Gu, Mingyu Ma et al. (23rd Feb. 2021). 'Strengthening polyethylene thermoplastics through a dynamic covalent networking additive based on alkylboron chemistry'. *Macromolecules* 54.4, pp. 1760–1766. ISSN: 0024-9297, 1520-5835. DOI: 10.1021/acs.macromol.0c02870.
- Weeks, John D., David Chandler and Hans C. Andersen (1971). 'Role of repulsive forces in determining the equilibrium structure of simple liquids'. *The Journal of Chemical Physics* 54.12, pp. 5237–5247. ISSN: 00219606. DOI: 10.1063/1.1674820.
- Winne, Johan M., Ludwik Leibler and Filip E. Du Prez (2019). 'Dynamic covalent chemistry in polymer networks: a mechanistic perspective'. *Polymer Chemistry* 10.45, pp. 6091–6108. DOI: 10.1039/C9PY01260E.
- Xia, Jianshe, Julia Ann Kalow and Monica Olvera de la Cruz (Oct. 2023). 'Structure, dynamics, and rheology of vitrimers'. *Macromolecules* 56.19, pp. 8080–8093. ISSN: 15205835. DOI: 10.1021/acs.macromol.3c01366.
- Zheng, Jie, Zhuang Mao Png, Shi Hoe Ng et al. (Dec. 2021). 'Vitrimer: current research trends and their emerging applications'. *Materials Today* 51, pp. 586–625. ISSN: 13697021. DOI: 10.1016/j.mattod.2021.07.003.

Entropic phase separation in vitrimer–polymer melts: supplementary information

Alexandros A. Rispo Constantinou ^{*1,2}, Bálint Magyari ^{1,3}, Giovanni Ianniruberto ¹,
Evelyne van Ruymbekke ², and Daniel J. Read ⁴

¹DICMaPI, Università degli Studi di Napoli Federico II, 80125 Naples, Italy

²BSMA, IMCN, Université catholique de Louvain, 1348 Louvain-la-Neuve, Belgium

³MSE, University of Crete, 70013 Heraklion, Greece

⁴School of Mathematics, University of Leeds, Leeds LS2 9JT, United Kingdom

*E-mail: alexandrosandreas.constantinou@unina.it

25th March 2026

A Full free-energy derivation

In this section, we provide a derivation for the free energy of the system when the assumption of ‘phantom’ cross-linker and stopper moieties is relaxed. For this fuller derivation, we will use a lattice argument on the four species comprising our system:

- (A) the homopolymer matrix, consisting of n_A chains of size N_A ;
- (B) the vitrimer backbone, similarly consisting of n_B chains of size N_B ;
- (C) the (difunctional) cross-linker moiety, n_C units of size N_C , connecting distinct stickers;
- (D) and the (monofunctional) stopper moiety (n_D, N_D), occupying any sticker not cross-linked.

We will begin with the usual Flory–Huggins entropy of mixing for these four species, then extend it to the cross-linked case. Note that we assume that cross-linker and stopper molecules are always attached to a sticker of the vitrimers; no sticker site is left unfilled. This assumption of stoichiometry reflects the structure of stably synthesised vitrimers (Röttger et al., 2017).

Imagine filling up a lattice with molecules of a given species i ; say the lattice has n_0 sites and a coordination number z . For the first molecule, occupying N_i sites, there are n_0 choices for the first occupied lattice site, z for the next, some number y – depending on the molecule’s flexibility – for the next, y again for the next, and so on until the end of the molecule. This molecule thus contributes $n_0 z y^{N_i-2} =: n_0 \zeta_i$ choices to the total configuration count. (We wrap several constants into the species-dependent flexibility factor ζ_i ; this allows us to do away with

special treatment of the cases $N_i = 1$ and $N_i = 2$.) We can repeat this procedure for all the other molecules, with one modification: as we progressively fill up the lattice, some of the lattice sites will be already occupied. We thus weight every new choice by the probability that the site is free at that step. Repeating for all molecules n_i of a given species i – yielding a factor $(n_0 \zeta_i)^{n_i}$ – and for all species in the mixture, we obtain a configuration count of

$$\Omega = \prod_{\text{species } i} (n_0 \zeta_i)^{n_i} \times \prod_{t=0}^{n_0-1} \mathbb{P}(\text{next site free after } t \text{ steps}). \quad (24)$$

Following the classic mean-field derivation of Flory (1953, § XII-1a), we set the probability that the next site is free to be the number of free sites after t steps, *i. e.*, $\mathbb{P}(t) = (n_0 - t)/n_0$. Simplifying and dividing by $n_i!$ for the Gibbs correction (indistinguishability within a species), we find

$$\Omega = \frac{n_0!}{n_0^{n_0}} \times \prod_{\text{species } i} \frac{(n_0 \zeta_i)^{n_i}}{n_i!}. \quad (25)$$

This is the configuration count for the Flory–Huggins mixture theory.

From this, we obtain the count for the cross-linked system by (i) allowing for all possible pairings of stickers, (ii) removing degrees of freedom due to moieties being attached, and (iii) claiming that the orientation of the cross-linker is immaterial. Item (iii) is easy, as it simply introduces n_C factors of $1/2$ into the overall count. Items (i) and (ii) are a bit more subtle, and require some care. Here we follow the argument of Dobrynin (2004) to compute the number of pairings and the loss of degrees of freedom. Since we have already corrected for the indistinguishability, we treat the C- and D-moieties as ordered in what follows.

We first count the cross-linked sticker pairs, then include the stoppers. Choose a first sticker (sn_B choices). The probability that the first cross-linker moiety starts on any of the x bondable sites adjacent to the first sticker is x/n_0 , as the moiety that could previously explore the whole volume is now restricted to lie on one of x sites. Here, x acts like a discretised bond volume. Then, the probability that any of the x sites on the other end of the C-moiety is occupied by another sticker is, by the mean-field approximation, $x \times (sn_B - 1)/n_0$. And this is one pair. Then we repeat: pick a sticker ($sn_B - 2$ choices), ask after the probability that it connects to the next C-moiety (x/n_0), take the probability of seeing a new sticker $x \times (sn_B - 3)/n_0$, repeat. After placing all C-moieties, we then pick our next new sticker out of a pool of $sn_B - 2n_C$ stickers, and note that the probability of seeing the first D-moiety is x/n_0 . Continuing this procedure until we have placed all D-moieties (thus covering all stickers), we obtain the product

$$sn_B \times x \times \frac{(sn_B - 1)}{n_0} \times \dots \times (sn_B - 2n_C + 1) \times x \times \frac{(sn_B - 2n_C)}{n_0} \\ \times (sn_B - [2n_C - 1]) \times \frac{x}{n_0} \times \dots \times 1 \times \frac{x}{n_0},$$

which collapses to $(sn_B)! \times (x/n_0)^{sn_B}$ (where we have used the assumption of stoichiometry $sn_B = 2n_C + n_D$ to simplify the exponent). Thus, putting everything together, we obtain an expression for the configuration count

$$\Omega = \frac{n_0!}{n_0^{n_0}} \frac{(sn_B)!}{2^{n_C}} \left(\frac{x}{n_0} \right)^{sn_B} \prod_{i=A}^D \frac{(n_0 \zeta_i)^{n_i}}{n_i!}. \quad (26)$$

Taking the negative logarithm, applying Stirling's formula, and dividing by the number of lattice sites n_0 , we obtain the dimensionless free energy per lattice site

$$\begin{aligned} f &:= (-TS)/(n_0 k_B T) \\ &= 1 + \frac{\log 2}{N_C} \phi_C - \frac{s\phi_B}{N_B} \log \left(\frac{xs\phi_B}{eN_B} \right) + \sum_i \frac{\phi_i}{N_i} \log \left(\frac{\phi_i}{eN_i \zeta_i} \right), \end{aligned} \quad (27)$$

where the volume fraction of a given species is calculated according to $\phi_i = N_i n_i / n_0$. Subtracting from the above expression any constants or terms linear in the concentration variables ϕ_i , we obtain the standard form of our free energy,

$$f = -\frac{s\phi_B}{N_B} \log \phi_B + \sum_i \frac{\phi_i}{N_i} \log \phi_i. \quad (28)$$

In these expressions, the volume fractions are related by the following system of equations:

$$\begin{bmatrix} 1 & 1 & 1 & 1 \\ 0 & sN_B^{-1} & -2N_C^{-1} & -N_D^{-1} \end{bmatrix} \begin{bmatrix} \phi_A \\ \phi_B \\ \phi_C \\ \phi_D \end{bmatrix} = \begin{bmatrix} 1 \\ 0 \end{bmatrix}. \quad (29)$$

A convenient choice of basis is the pair (ϕ, ψ) defined by

$$\phi = 1 - \phi_A \quad \text{and} \quad \psi = \frac{2N_B}{sN_C} \phi_C, \quad (30)$$

since ϕ is the vitrimer volume fraction and both ϕ and ψ are of comparable magnitude in the phase-space domain. (Indeed, the bounds $0 \leq \phi \leq 1$ and $0 \leq \psi \leq (1 + sN_C/2N_B)^{-1} \phi$ form the boundary of the domain.) Note that, following the inclusion of the cross-linker and stopper moieties into the volume balance in eq. (29), we lose the nice relationship $p = \psi/\phi$, replacing it instead with

$$p = \frac{(N_B + sN_D)\psi}{N_B \phi + s(N_D - N_C/2)\psi}. \quad (31)$$

Despite the increased complexity of this expression, lines of constant p continue to be lines of constant ratio ψ/ϕ .

A.1 Network cycles

What part of the above argument suggests correct treatment of cycles? When we invoked the mean-field approximation, we claimed that the probability that a given site was occupied by a sticker was $(sn_B - u)/n_0$, where u is the number of previously used-up stickers. Let us make a distinction: when we find a new sticker, it can either be on a cluster disconnected from the first sticker (with probability P_{dis}) or already connected to it through some path (with probability $P_{\text{con}} = 1 - P_{\text{dis}}$). In the case that the new sticker is completely disconnected, then it can explore the whole space, so the probability of seeing a sticker of this type is $P_{\text{dis}} \times (sn_B - u)/n_0$ as before. If instead it is somehow connected, it is constrained to some local neighbourhood n_* . Then the

expected number of stickers in this neighbourhood is, *by the mean-field approximation*, just the overall number of stickers reduced by the local neighbourhood size: $(sn_B - u) \times n_*/n_0$. Hence the the probability of seeing a sticker of this second type is $P_{\text{con}} \times (sn_B - u)/n_* \times n_*/n_0$. Thus the total probability of seeing a sticker in the given site is

$$\left(P_{\text{dis}} \times \frac{sn_B - u}{n_0} \right) + \left(P_{\text{con}} \times \frac{sn_B - u}{n_*} \times \frac{n_*}{n_0} \right) = \frac{sn_B - u}{n_0},$$

exactly the expression we used before. This is an established property of such models, stated *e. g.* by Tanaka (2022, p. 18).

A.2 Links to the same chain

Technically, there is a slight contradiction, since the theory as stated should disallow stickers from connecting to stickers on the same chain. In practice, the error is vanishing. We compute it as follows: as we go along creating our network, each choice of sticker should exclude the $s - 1$ other stickers on the same chain. Thus we multiply the number of yet-unused stickers by the probability, for each sticker, that the chosen partner sticker is on a different chain:

$$\left(1 - \frac{s-1}{sn_B} \right)^{n_C} \xrightarrow{n_B \rightarrow \infty} \exp\left(-\frac{s-1}{2} p\right).$$

This is vanishingly small when we compute the intensive free energy $f = -\log(\Omega)/n_0$.

A.3 Nearest-neighbour correction

We provide also the nearest-neighbour correction for the four-species system. Since the derivation is essentially identical to that of eq. (5) in the main body of the paper, we proceed in telegraphic style. The entropic partition function is given by the expression

$$\begin{aligned} \Omega = \frac{n_0!}{n_0^{n_0}} \left[\prod_i \frac{(n_0 \zeta_i)^{n_i}}{n_i!} \right] \times \mathbb{P}[L_{N_B/s}]^{\frac{1}{2} q sn_B} \left[\frac{(s - \frac{1}{2} qs)!}{(\frac{1}{2} qs)! (s - qs)!} \right]^{n_B} \\ \times \frac{(sn_B - qsn_B)!}{2^{(n_C - \frac{1}{2} qsn_B)}} \frac{n_C!}{(n_C - \frac{1}{2} qsn_B)!} \left(\frac{x}{n_0} \right)^{(sn_B - \frac{1}{2} qsn_B)}, \end{aligned} \quad (32)$$

recalling that $n_0 = \sum_i N_i n_i$ and $sn_B = 2n_C + n_D$. In these expressions, the index i runs over all four moieties A, B, C, and D. Taking the logarithm and minimising over q gives the intensive free energy

$$\begin{aligned} f = -\mathfrak{H} \left(\frac{s\phi_B}{N_B} - \frac{q}{p} \frac{\phi_C}{N_C} \right) + \sum_i \frac{\mathfrak{H}(\phi_i)}{N_i} \\ + \left[\mathfrak{H}(1 - q/p) + \mathfrak{H}(q/p) + \frac{q}{p} \log \left(\frac{2N_B}{esk} \right) \right] \frac{\phi_C}{N_C}, \end{aligned} \quad (33)$$

with $\mathfrak{H}(z) := z \log(z)$ and $q \approx kp/(k + 2\phi_B)$. For numerical work, it is convenient to re-write this in terms of (ϕ, ψ) as defined in eq. (30), and use the rescaled free energy $N_B f/s$.

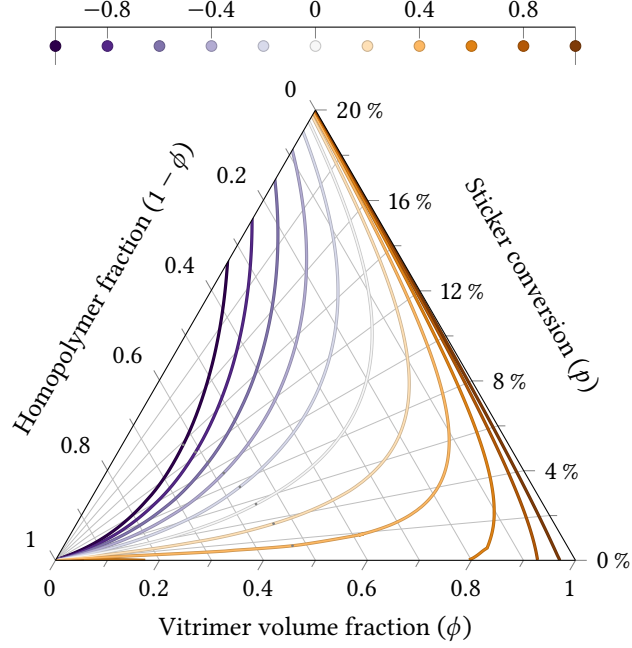


Figure I: Effect of an energetic interaction ($dp_A = dp_B = 500$, $s = 50$, $k \approx 0.30$; χ varying). *The Flory interaction parameter between backbones and dioxaborolanes controls the position of the binodal line.*

B Energetic interactions

It is rare in real melts to find a system which is truly in theta-solvent conditions. What consequence does adding an interaction energy between monomers of different species bring? While the true effect of the backbone chemistry on vitrimer mechanics is still unclear (Ge and Evans, 2025), we believe the exploration of a toy model, based on the Flory–Huggins interaction parameter, is helpful as a first approach to the subtleties of including chemistry into our predictions.

B.1 A first look

It is in the non-phantom framework — where all four moieties have independent existence — that the inclusion of an energetic interaction is most meaningful. In the abstract, one could provide interactions between all $4(4 - 1)/2 = 6$ possible combinations of moiety. In a concrete example, however, like that of a dioxaborolane-based stopper–cross-linker pair, that number halves. If, furthermore, the vitrimer is of the same backbone as the polymer matrix, the simplest correction to the free energy might be of the form $\Delta f = \chi(\phi_A + \phi_B)(\phi_C + \phi_D)$, namely as a Flory interaction parameter χ taken between unlike chemical species. This is the most sensible expression in the limit as the inter-function spacing dp_B/s grows, since then contacts between non-identical chemical elements become increasingly rare. Using the expression $\chi\phi_A(1 - \phi_A)$

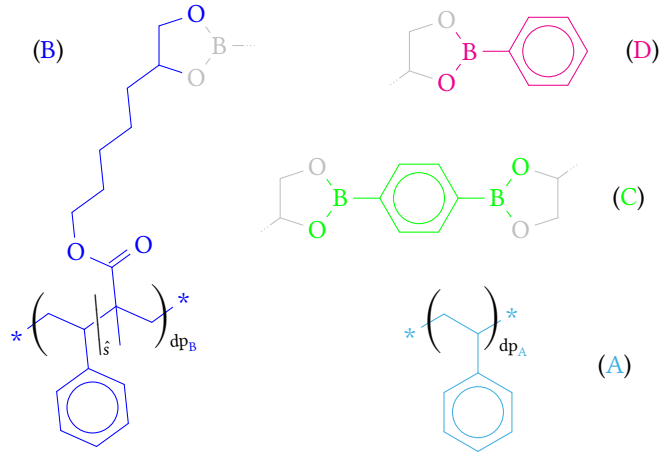


Figure II: Chemistry of a polystyrene/dioxaborolane vitrimer melt.

— which sets homopolymer chains against all components of the vitrimer — while seeming natural at first, would vastly overestimate the enthalpic repulsion when dp_B/s is large. The interaction parameter χ will have an effect on the binodal when it is comparable in size to the stable, Flory–Huggins part of the free energy expression. Since $\phi_C \sim s\phi_B/N_B$, and the stable term in eq. (28) scales as $1/N_B$ (assuming N_C and N_D are roughly unity, and $N_A \sim N_B$), we expect this to occur when $s\chi \sim 1$.

Implementing Δf for $\chi \in \{1, 0.8, \dots, -1\}$ gives the diagrams in fig. I. (Parameter values $dp_i = 500$, $s = 50$ were chosen to keep algorithm run-time low.) We see that the effect of the interaction parameter is fairly straightforward: the binodal advances for $\chi > 0$ and recedes for $\chi < 0$. The natural scale which varies the binodal, $\chi \sim 10^{-1}$, is consistent with the interpretation that the relevant scaling for the interaction parameter is $\chi \sim 1/s$.

B.2 Splitting the molecules

Figure II shows the chemical structure of a polystyrene-based vitrimer–homopolymer melt with dioxaborolane-based cross-linker and stopper, categorised into the four species A, B, C and D. The cutting-point between B and C/D is chosen to be the point where the chemical bonds break during a cross-link exchange interaction. We note, however, that splitting C/D from B at a different point than that indicated in fig. II may allow the expression $\chi(\phi_A + \phi_B)(\phi_C + \phi_D)$ better to capture the enthalpic behaviour of these materials. An example alternative split is shown in fig. III. The choice of optimal split can only be made with a detailed understanding of the chemistry involved.

Incidentally, a split can always be chosen such that $N_B = dp_B$ (leaving, in our example material, $N_C = 3 + 3/52$ and $N_D = 2 - 5/52$), which does simplify some algebra, but is unlikely to correspond to anything physically meaningful in terms of the chemistry.

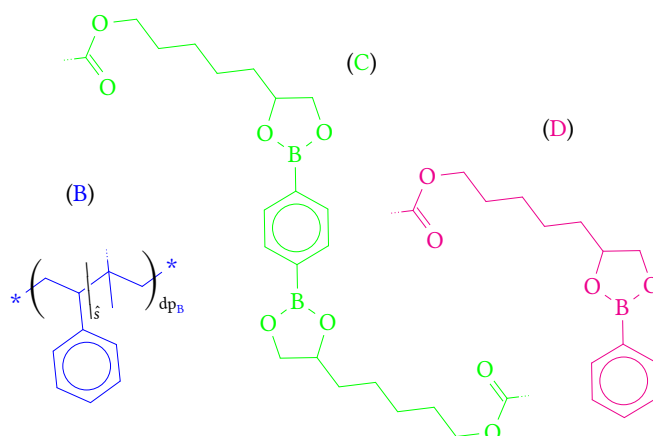


Figure III: Alternative method of chopping up a polystyrene vitrimer with dioxaborolane functions into species B, C and D.

B.3 Globules and micro-phase segregation

The true effect of an energetic interaction, however, is likely to be more complicated than the simple addition of a term to the free energy. In the presence of a repulsive interaction between dioxaborolane and polystyrene, for example, we would expect the formation of globule-like structures or micro-phase separation in the vitrimer chains — especially when the vitrimer is dilute in the polymer matrix, when also assumptions of the mean-field theory begin to weaken. The free energy in these regimes then needs to be treated differently, for example by assuming from the outset the formation of globular structures for vitrimer chains in the derivation of the free energy (Dobrynin, 2004; Semenov and Rubinstein, 1998). As concerns micro-phase separation, however, this is likely beyond the predictive power of a theory such as this, which is based entirely on the assumption of a mean field.

C Cross-linker of arbitrary functionality

In this section, we provide a calculation of the system entropy when the cross-linker is not difunctional, but has an arbitrary functionality $r \geq 2$. For simplicity, we will return to the ‘phantom’ approximation, where cross-linker and stopper do not occupy any physical volume. The calculation is a trivial generalisation of the difunctional case when cross-links are only between different chains, but requires some care when cross-links are allowed to involve stickers from the same chain. We will again approximate the same-chain entropy with its leading-order contribution, namely when all local bonds are between runs of successive (‘nearest-neighbour’) stickers. Longer-range bonds are suppressed polynomially, scaling as the inter-sticker distance to the power of $-3/2$.

Define q_i as the proportion of stickers involved in a run of i successive stickers on one chain

all attached to the same cross-linker. Then defining

$$q := \sum_{i=2}^r q_i \quad \text{and} \quad \bar{q} := \sum_{i=2}^r \frac{1}{i} q_i,$$

we use a ‘stars-and-bars’-type argument within each vitrimer chain with $r - 1 = \{2, \dots, r\}$ different types of ‘bars’, each occurring respectively q_i/i times in the chain. The total number of objects (‘stars’ plus ‘bars’) is $(s - qs) + \bar{q}s$, giving a combinatorial factor

$$\frac{[s(1 - q + \bar{q})]!}{[s(1 - q)]! \prod_{i=2}^r \left(\frac{1}{i} s q_i\right)!}. \quad (34)$$

This configuration occurs with probability $\mathbb{P}[L_{N/s}]^{s(q-\bar{q})}$, where the exponent is the number of loops formed by attachment to the cross-linker (namely, $i - 1$ for every cross-linker combining i successive stickers).

We then have to place all remaining stickers. We use a similar picture to the one in section 2.1, but with more types of cross-linker: in brackets those fully free, and in parentheses those already partially attached due to nearest-neighbour cross-linking. The total number of asterisks to place is $sn(1 - q)$.

$$\overbrace{() \cdots ()}^{n \frac{sq_r}{r}} \quad \overbrace{(*) \cdots (*)}^{n \frac{sq_{r-1}}{r-1}} \quad \cdots \quad \overbrace{(*, \dots, *) \cdots (*, \dots, *)}^{n \frac{sq_2}{2} \text{ have } r-2 \text{ sites free}} \quad \Bigg| \quad \overbrace{[* \cdots *] \cdots [* \cdots *]}^{sn(\frac{p}{r}-\bar{q}) \text{ non-local}} \quad \Bigg| \quad \overbrace{** \cdots **}^{sn(1-p) \text{ free}}$$

This picture allows us to immediately write down the remaining combinatorial factor,

$$\frac{1}{r!^{sn(\frac{1}{r}p-\bar{q})} \prod_{i=2}^r (r-i)!^{sq_i/i}} \times \frac{[sn(1-q)]!}{[sn(1-p)]! [sn(\frac{1}{r}p-\bar{q})]!} \quad (35)$$

where we have divided by permutations of stickers within parentheses or brackets, along with permutations of the brackets or of the free stickers. We have *not* divided by permutations of the parentheses, as these are not interchangeable: a cross-linker combining i nearest-neighbour stickers on one chain is distinct from a cross-linker combining i on another. The probabilistic weight associated with eq. (35) has exponent given by the number of bound asterisks in the picture, yielding $(x/n_0)^{sn((1-\frac{1}{r})p+\bar{q}-q)}$. Combining together eqs. (34) and (35), we find a partition function

$$\begin{aligned} \frac{\Omega}{\Omega_{\text{FH}}} &= \frac{[s(1 - q + \bar{q})]!^n \left(\frac{1}{4} kxs/N\right)^{sn(q-\bar{q})}}{[s(1 - q)]!^n \prod_{i=2}^r (sq_i/i)!^n} \\ &\times \frac{[sn(1 - q)]! \left(\frac{x}{n_0}\right)^{sn[(1-\frac{1}{r})p-q+\bar{q}]}}{r!^{sn(\frac{1}{r}p-\bar{q})} [sn(1 - p)]! [sn(\frac{1}{r}p - \bar{q})]! \prod_{i=2}^r (r - i)!^{sq_i/i}} \end{aligned} \quad (36)$$

where we have substituted $\mathbb{P}[L_{N/s}] = \frac{1}{4} kxs/N$.

Nearest-neighbour cross-links with runs of more than two elements are exponentially suppressed as they involve the factor $\mathbb{P}[l_{N/s}]$ raised to the number of loops. Therefore, we approximate eq. (36) with its leading-order behaviour, namely where $q_i = 0 \forall i > 2$. Performing that simplification and computing the free energy gives the expression

$$\begin{aligned} \frac{N}{s} f = & \frac{1}{s} \left(\mathfrak{H}(\phi) + \frac{N}{M} \mathfrak{H}(1 - \phi) \right) + \mathfrak{H}(\phi - \psi) \\ & + \frac{1}{2} \mathfrak{H} \left(\frac{2}{r} \psi - q\phi \right) - \mathfrak{H} \left(\left[1 - \frac{1}{2} q \right] \phi \right) \\ & + \frac{1}{2} \mathfrak{H}(q\phi) + \frac{1}{2} q\phi \log \left(\frac{4/e}{kr(r-1)} \right) \end{aligned} \quad (37)$$

as required. This is minimised when

$$\frac{(2-q)q}{2p-rq} = (r-1) \frac{k}{2\phi} \quad (38)$$

leading to the linearisation

$$q \approx \frac{2(r-1)kp}{r(r-1)k + 4\phi}.$$

Inspection shows that small, reasonable values of the cross-linker functionality ($r \lesssim 10$) give near-identical expressions for the free energy in eq. (37) equivalent to rescaling $\phi \mapsto \phi/(r-1)$, and are thence not expected to yield qualitatively different results for the bulk of the phase diagram.

In contrast with the case $r = 2$, however, eq. (38) for general r does *not* yield the correct behaviour $q \rightarrow p$ as $\phi \rightarrow 0$ (dilute vitrimer limit). This is because cross-linking runs of more than two successive stickers gain in importance when associations are primarily intra-chain, and need to be added back into the model, reversing the approximation immediately preceding eq. (37).

D Additional plots

Figures 6 to 8 in the main text are for $\phi = 0.5$. The corresponding plots for all remaining simulated values of ϕ are given in this section, in figs. IV to VI respectively. These show: the normalised spatial correlation functions (figs. 6 and IV), the normalised density variance (figs. 7 and V), and the data for the measurement of the percolation transition (figs. 8 and VI).

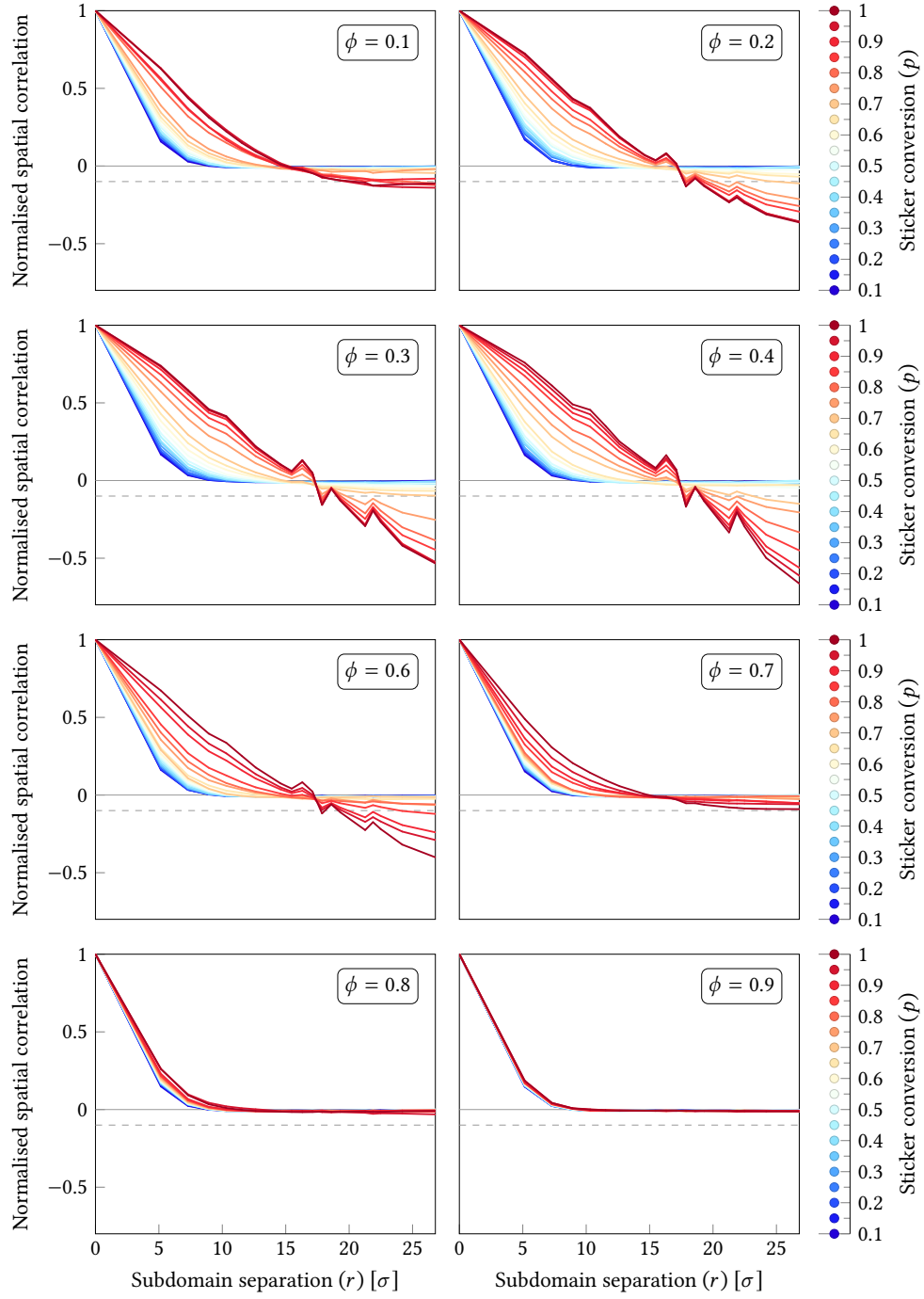


Figure IV: Normalised spatial correlation as a function of subdomain separation for ϕ between 0.1 and 0.9 excluding 0.5 (for which see fig. 6).

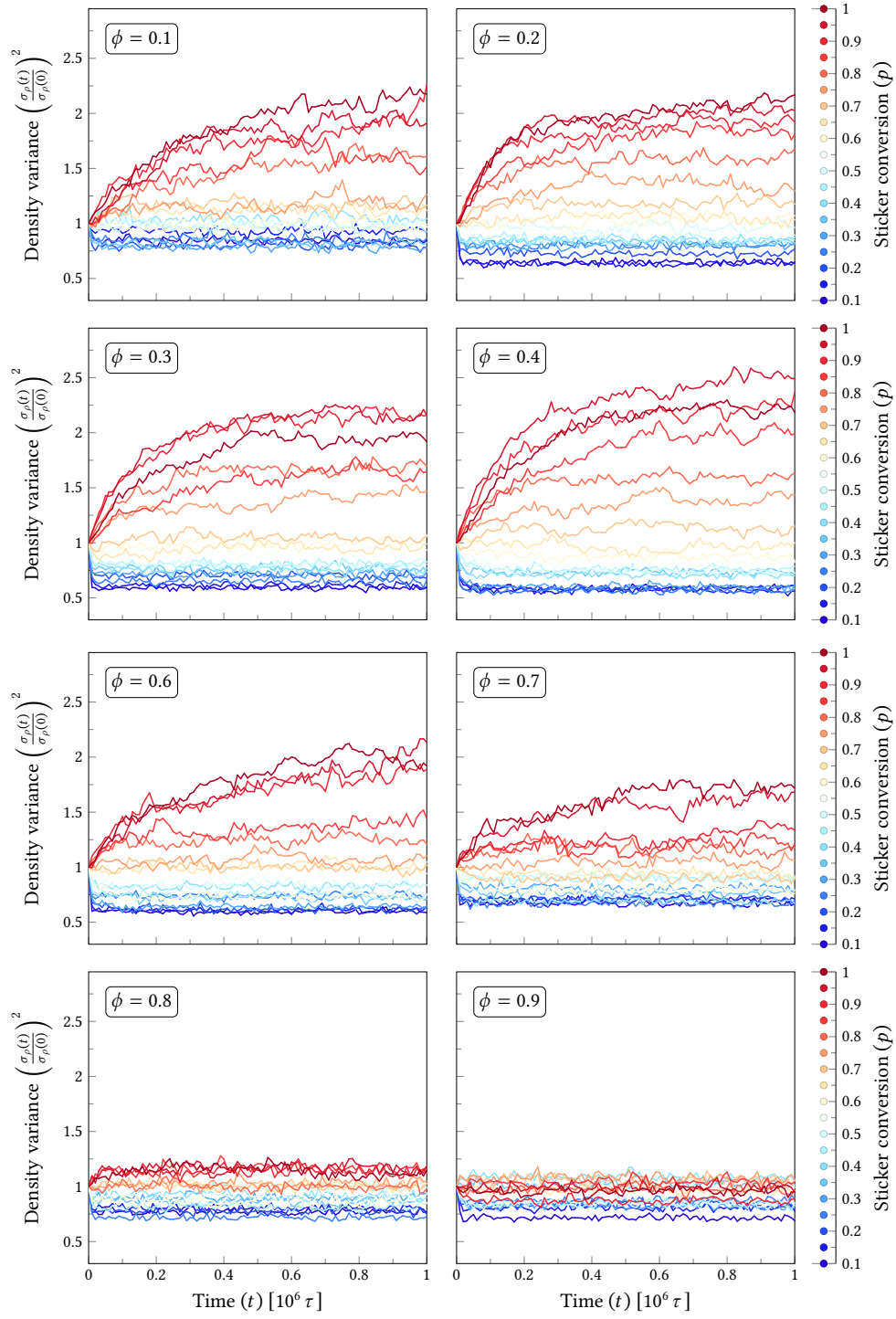


Figure V: Normalised density variance as a function of simulation time for ϕ between 0.1 and 0.9 excluding 0.5 (for which see fig. 7).

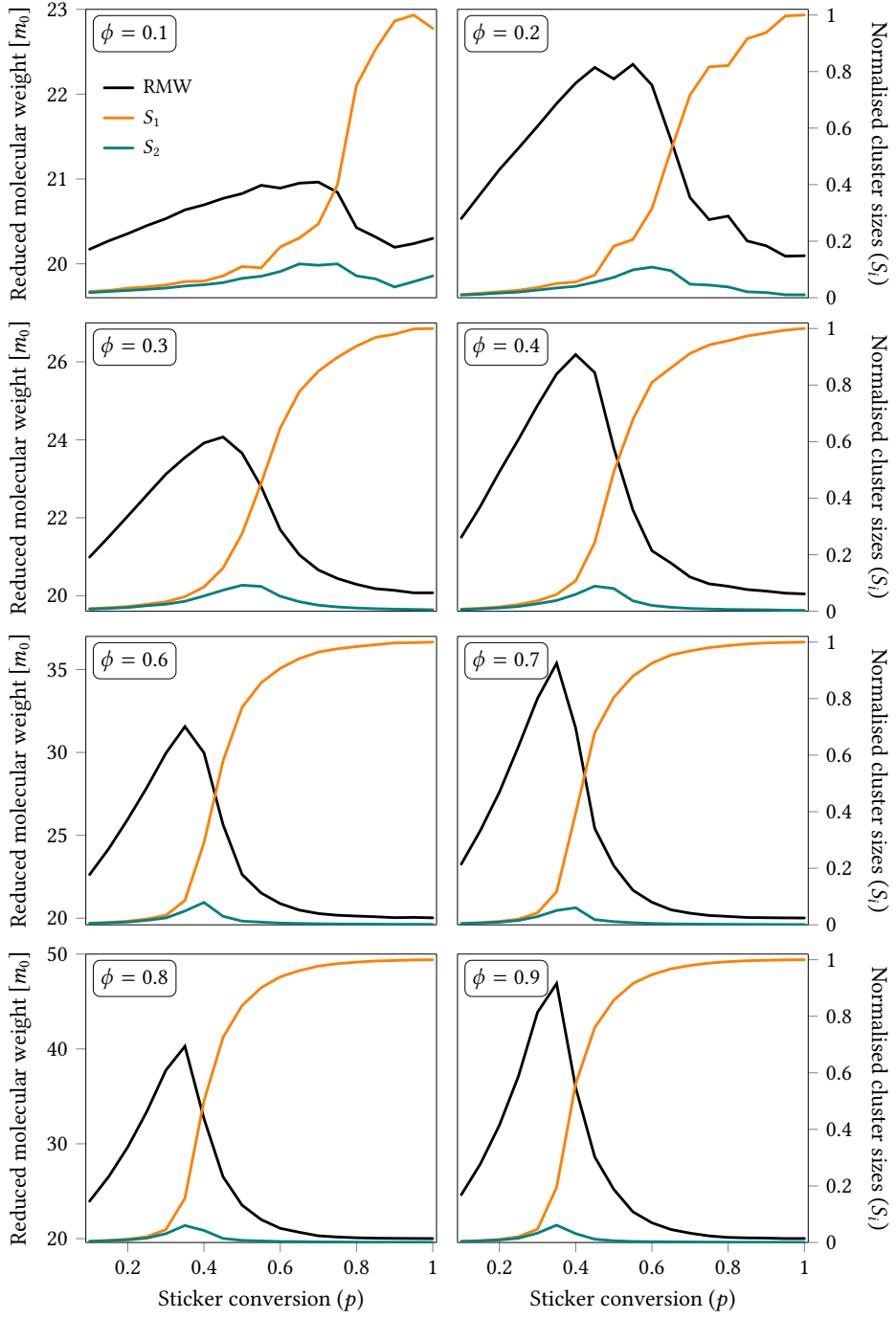


Figure VI: Data required for the measurement of the percolation transition, for ϕ between 0.1 and 0.9 excluding 0.5 (for which see fig. 8).